Antiviral Research 254 (2026) 106514

Contents lists available at ScienceDirect

Antiviral Research

journal homepage: www.elsevier.com/locate/antiviral

γ-Monoalkyl triphosphate analogues of acyclic nucleoside phosphonates inhibit SARS-CoV-2 replication *in vitro* by inducing dissociation of the minimal replication-transcription complex

Paolo Malune [a], Giuliano Kullik [b], Xiao Jia [b,c], Gyde Bandowski [b], Francesca Esposito [a], Antonio Lupia [a], Simona Distinto [a], Elias Maccioni [a], Chris Meier [b,d,*], Enzo Tramontano [a,**]

[a] Department of Life and Environmental Sciences, University of Cagliari, Cittadella Universitaria di Monserrato, Cagliari, 09124, Italy
[b] Department of Chemistry, Organic Chemistry, Faculty of Sciences, University of Hamburg, Martin-Luther-King-Platz 6, Hamburg, 20146, Germany
[c] State Key Laboratory of Drug Research, Shanghai Institute of Materia Medica, Chinese Academy of Sciences, Shanghai, 201203, China
[d] Centre for Structural Systems Biology (CSSB), Hamburg, DESY Campus, Notkestrasse 85, Hamburg, 22607, Germany

ARTICLE INFO

Keywords:
RNA-dependent RNA polymerase
SARS-CoV-2
Drug discovery
Nucleotide analogues
Complex dissociation
Protein-protein interaction

ABSTRACT

Nucleoside triphosphate analogues in which the γ-phosphate has two different non-cleavable lipophilic alkyl residues were observed to potently inhibit HIV-1 replication *in vitro*. We report that a series of γ-monoalkyl triphosphate analogues of acyclic nucleoside phosphonates inhibits the RNA-dependent RNA polymerase (RdRp) function of the SARS-CoV-2 nsp12 protein. These nucleotide analogues were synthesized with multiple nucleobase derivatives, sharing one alkyl group of two different lengths on the γ-phosphonate. The enzymatic PAGE-based assay of SARS-CoV-2 nsp12 with cofactors nsp7/8 revealed IC_{50} values in the low micromolar range, whose potency depended on the length of the alkyl group, with no incorporation of the analogues and complete loss of enzymatic function. Competition assay revealed that the tested nucleotide analogues do not compete with the natural triphosphate nucleotides independently of sequence complementarity, hence acting as non-nucleoside inhibitors. By multiple techniques, we demonstrated that the inhibitors induce the dissociation of the nsp7 cofactor from the nsp12 subunit. Molecular docking and molecular dynamic simulations supported this mechanism identifying a putative binding site in an interface cavity between nsp12-nsp8 and nsp7, where the compound forms both hydrogen bonds and hydrophobic interactions. Different prodrugs of the most potent nucleotide analogues were synthesized and showed inhibitory activity against SARS-CoV-2 replication in cell culture.

1. Introduction

SARS-CoV-2 possesses a large RNA genome of approximately 30 kb that encodes 16 non-structural proteins, 4 structural proteins, and several accessory proteins (Steiner et al., 2024). Among the non-structural proteins, SARS-CoV-2 encodes nsp12 as its RdRp, a key enzyme required for viral genome replication and transcription, displaying the conserved right-hand architecture typical of RNA and DNA polymerases, with the Palm, Thumb, and Fingers subdomains (Malone et al., 2022). Together with the cofactors nsp7 and nsp8, nsp12 forms the minimal replication–transcription complex (RTC), and participates in template backtracking, which supports proofreading during RNA synthesis (Malone et al., 2022). Despite the availability of vaccines and antiviral agents SARS-CoV-2 global spread still represents a significant threat, with about 7.1 million COVID-19-related deaths, as of January 2026 (World Health Organization, 2025). Numerous known nucleoside analogues were tested for their ability to inhibit SARS-CoV-2 RdRp activity and viral replication, with several compounds showing promising results *in vitro* after incorporation by the polymerase by diverse mechanisms of action. While the nucleotide analogue prodrug remdesivir

* Corresponding author. Department of Chemistry, Organic Chemistry, Faculty of Sciences, University of Hamburg, Martin-Luther-King-Platz 6, 20146, Hamburg, Germany.
** Corresponding author.
E-mail addresses: chris.meier@uni-hamburg.de (C. Meier), tramon@unica.it (E. Tramontano).

https://doi.org/10.1016/j.antiviral.2026.106514
Received 18 March 2026; Received in revised form 3 July 2026; Accepted 16 August 2026
Available online 17 August 2026

continues to be evaluated for its clinical efficacy (Okoli et al., 2021, 2024; Zur et al., 2024), molnupiravir has been withdrawn from the European market following a negative risk–benefit assessment by the European Medicines Agency (European Medicines Agency, 2023). Moreover, increasing evidence suggests that molnupiravir treatment may promote the emergence of new SARS-CoV-2 variants by elevating the viral mutation rate, as indicated by the presence of drug-associated mutational signatures in circulating viral genomes (Kabinger et al., 2021).

Other nucleobase(side) analogues, such as favipiravir (T-705), its non-fluorinated analogue T-1105 and ribavirin triphosphates, were shown to be incorporated into the nascent RNA strand by the SARS-CoV-2 RdRp, but with a lower efficiency compared to natural nucleotides, consistent with the relatively high EC_{50} values against viral replication in cell-based assays (Gordon et al., 2020).

These findings strengthen the use of the viral RdRp as a target for the identification of new inhibitors effective against SARS-CoV-2 and other human Coronaviruses. The longstanding limitation of nucleoside analogues is their poor delivery and stability *in vivo*, due to the fast clearance of the compounds, high hydrophilicity, and metabolic bottleneck associated with their activation. In fact, nucleoside analogues require phosphorylation by cellular kinases, that can be relatively slow and have a limited specificity of target (De Clercq, 2004; Jia et al., 2020a). An alternative strategy emerged from early evidence of antiviral activity associated with phosphonoacetic acid, which stimulated the search for more stable analogues (Clercq and Holý, 2005). This effort culminated in the development of acyclic nucleoside phosphonates by Holý and co-workers in the 1980s. These compounds comprise a chemically stable phosphorus-carbon-bond, generating metabolically resilient nucleotide surrogates that behave as monophosphate mimics. As examples, (*R*)-9-(2-(phosphonomethoxy)propyl)adenine (*R*)-PMPA **1** (tenofovir), an acyclic nucleotide analogue of dAMP, 9-(2-(phosphonomethoxy) ethyl)adenine PMEA **2** (adefovir), and (*S*)-3-hydroxy-2-phosphonomethoxypropylcytosine HPMPC **3** (cidofovir) still require two sequential phosphorylation steps to form the triphosphate analogue that acts as active species to block HIV reverse transcriptase (HIV-RT) (Balzarini et al., 1993; Ray, 2005). To address poor membrane diffusion due to the charged phosphonate group, lipophilic prodrug strategies were introduced (Jia et al., 2024; Zhao et al., 2020). The prodrug forms of (*R*)-RMPA **1** are tenofovir disoproxil fumarate (TDF **5**) and tenofovir alafenamide fumarate (TAF **5**) that are potent drugs used in HIV and HBV therapy (Fig. 1) (Clercq et al., 1987). In addition to their antiviral activities, acyclic nucleoside phosphonates also proved active as anti-tumor agents, e.g. (*S*)-HPMPC (Clercq et al., 1999).

Fig. 1. *Chemical formulae of known acyclic phosphonate nucleoside analogues as well as two prodrugs of (R)-PMPA.*

To overcome the limitations coming from the cellular phosphorylation of nucleoside monophosphate analogues, a series of triphosphate nucleotide analogues with a single or double noncleavable γ-alkyl-phosphonate moiety, in place of the natural γ-phosphate group, were developed. These nucleotide analogues, especially the d4T derivatives, were initially evaluated against HIV-1 and HIV-2 reverse-transcriptase (RT), demonstrating to be incorporated by the enzyme into the nascent DNA strand in a primer-elongation assay, inducing immediate chain termination (Jia et al., 2020b, 2023; Zhao et al., 2020). These analogues showed the ability to cross the cell membrane due to a partial mask of

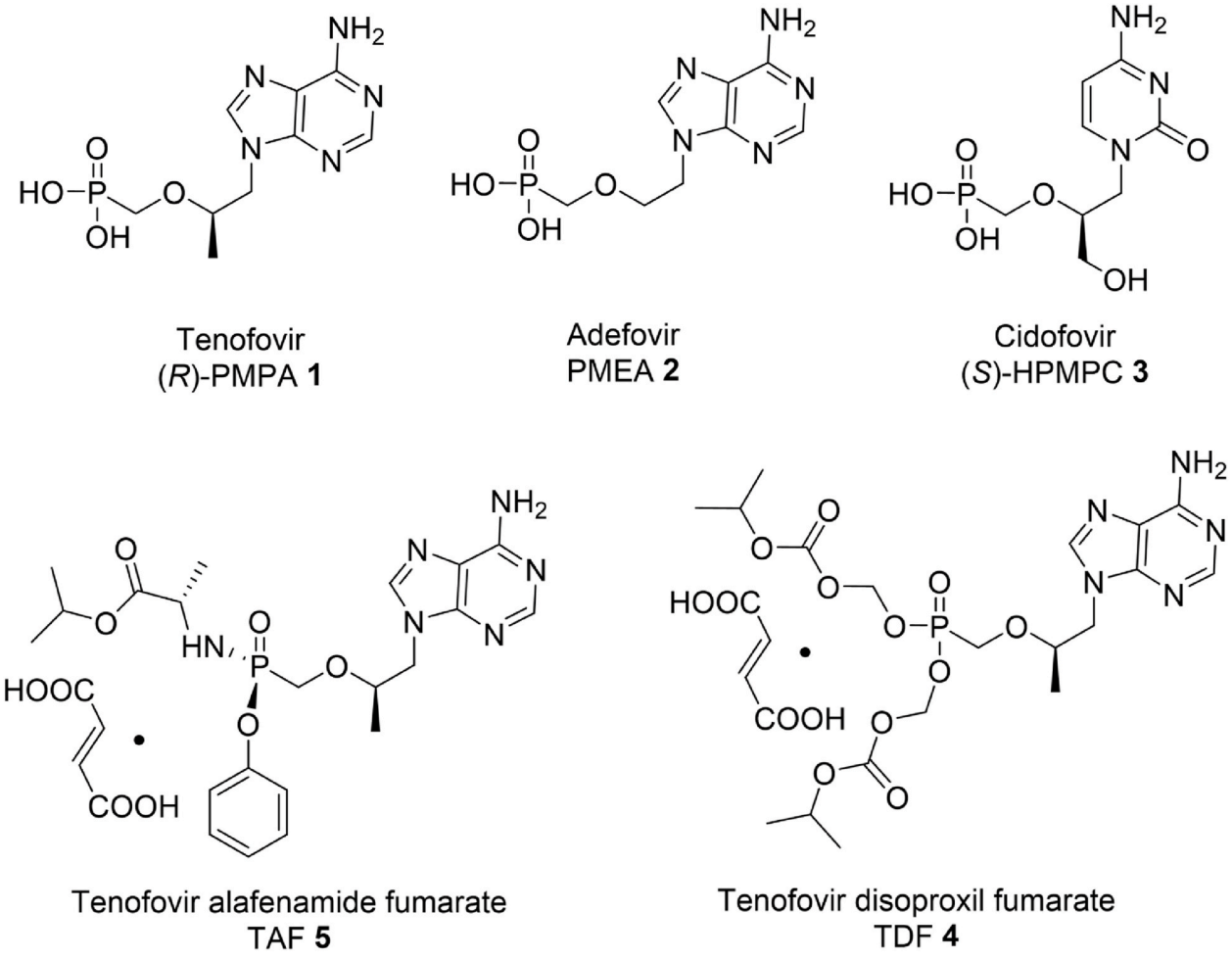

Fig. 1. Structure of known acyclic phosphonate nucleoside analogues.

their hydrophilic phosphate groups by the alkyl moieties. Notably, the introduction of an acyloxybenzyl or alkoxycarbonyloxybenzyl bio-reversible mask group at the γ-phosphate (Tri*PPP*ro compounds, namely prodrugs of triphosphate analogues, developed to bypass all cellular phosphorylation steps), increases molecular lipophilicity and results in a potent *in vitro* inhibition of HIV-1 and HIV-2 replication (Jia et al., 2020b).

In this work, we explored the ability of a series of γ-monoalkylated triphosphate analogues of acyclic nucleoside phosphonates to inhibit SARS-CoV-2 RdRp activity, in light of previous results obtained on the

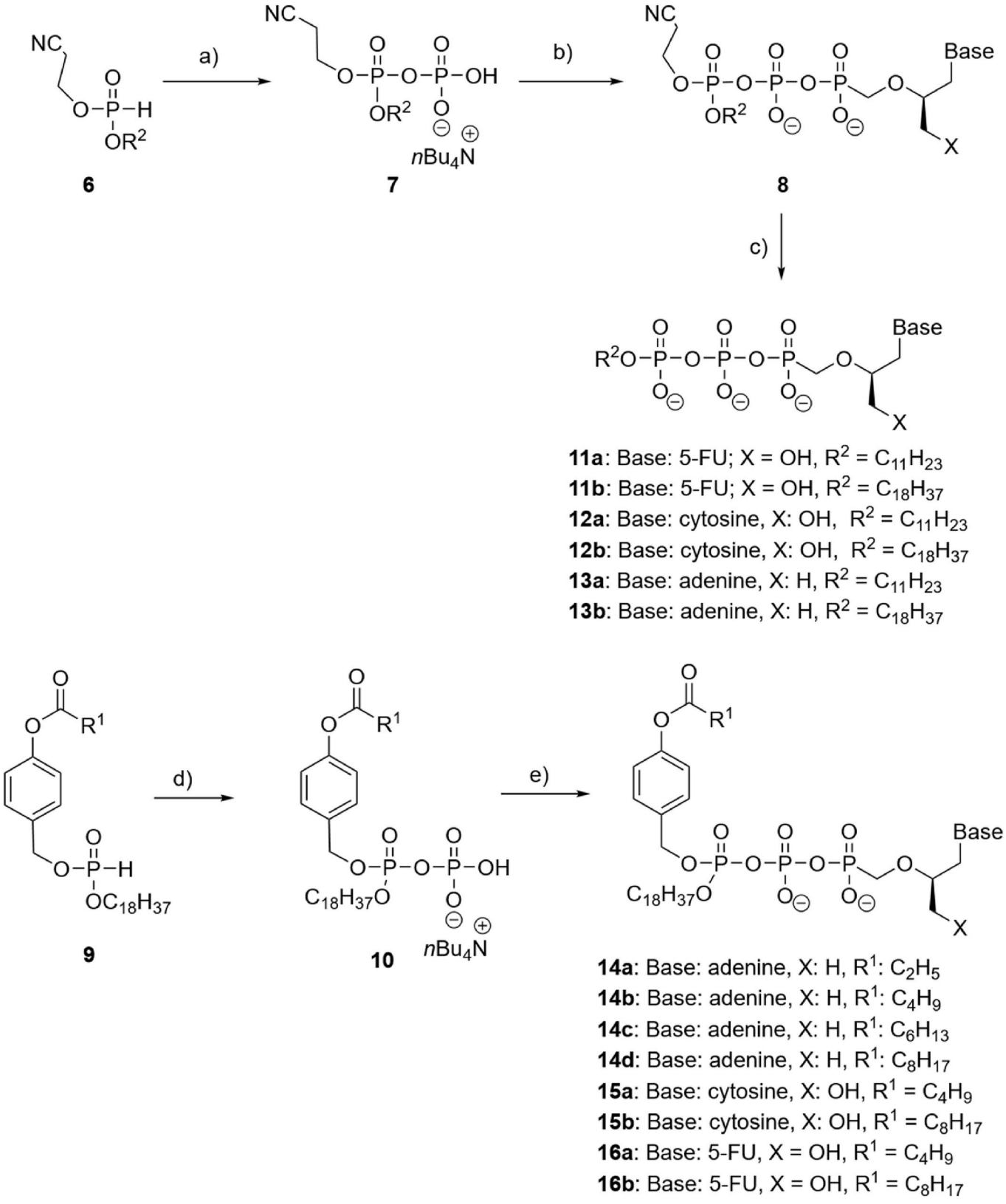

Fig. 2. Structure and synthesis of γ-monoalkyl triphosphate analogues of acyclic nucleoside phosphonates.

inhibition of HIV replication by such (*R*)-PMPA (tenofovir) and (*S*)-HPMPC (cidofovir) triphosphate derivatives (Jia et al., 2020a, 2023). This study extends and integrates results previously reported in the authors' doctoral dissertations (Kullik, 2023; Malune, 2025). We identified what appears to be a previously unreported mechanism of action, in which the nucleotide analogue induces the dissociation of the subunits of the minimal RTC, therefore impairing the polymerase's ability to catalyze viral RNA synthesis. The corresponding γ-acyloxybenzyl-prodrugs of the monoalkylated nucleotides analogues showed promising activity against SARS-CoV-2 replication *in vitro*, although further optimization of delivery has to be addressed to further enhance their antiviral potential.

2. Materials & methods

2.1. Chemistry

All experiments involving water- or air-sensitive compounds were conducted under dry conditions (nitrogen atmosphere). Anhydrous solvents were purchased from Acros Organics or dried by a MBraun (MB SPS-800)-System. Reagents were purchased from various commercial providers as described in reference (Jia et al., 2024). Commercially available reagents and solvents were used without further purification. (*S*)-HPMPC and the (*S*)-HPMPFU were prepared according to a literature procedure (Brodfuehrer et al., 1994). Evaporation of solvents (ethyl acetate, petroleum ether 50-70, CH_2Cl_2, acetone, and CH_3OH) was carried out on a rotary evaporator under reduced pressure or using a high-vacuum pump. Chromatography was performed with silica gel 60 M (0.04-0.063 mm, Macherey-Nagel) or using MN RS 16 C_{18} ec, RS 40 C_{18} ec or RS 120 C_{18} ec columns on an Interchim Puriflash 430 system. All high-performance liquid chromatography (HPLC) data were recorded and analyzed with OpenLab CDS software either on an Agilent Technologies 1260 Infinity II with following parts: 1260 Quat Pump VL, 1260 Vialsampler, 1260 DAD. Samples were measured with the following method: CH_3CN gradient in 2 mM tetrabutylammonium acetate (TBAA) buffer (pH 6.0); 0-20 min: 5-80%, flow 1 mL; from 20 to 30 min isocratic (20% TBAA, 80% CH_3CN), 30-33 min TBAA in CH_3CN gradient (80-5%), 33-38 min isocratic (95% TBAA, 5% CH_3CN; column: Nukleodur 100-5 C18 ec (Macherey Nagel), UV-detection at wavelength of 220 nm, 260 nm or 275 nm). All target compounds were analyzed for purity by NMR spectroscopy and RP-HPLC−UV. All NMR spectra were recorded on Bruker instruments Avance I 400 and Avance III 600. All chemical shifts (δ) were given in ppm and calibrated on solvent signals. MALDI mass spectra were recorded on an ultrafleXtreme MALDI-TOF-TOF mass spectrometer by Bruker Daltonik with 9-AA as matrix. The high-resolution ESI mass spectra were recorded on an Agilent 6624 Accurate-Mass TOF mass spectrometer by Agilent Technologies.

The syntheses and characterization of compounds **6** (19,21), **9** (19,21) (Fig. 2) and tenofovir containing compounds **13a**,**b**, **14a-d** were described previously (Jia et al., 2024). The analytical data were identical to the previously reported. NMR spectra of representative compounds are reported in Supplementary Fig. S1.

2.2. Preparation of γ-alkyl-modified nucleoside phosphonate-DPs 11 and 12

The compounds were prepared according to the general procedures given in references (Kullik, 2023; Jia et al., 2024) using (β-cyanoethyl)-undecanoyl- or octadecanoyl-*H*-phosphonate **6** (1.0 equiv.) yielding β-cyanoethyl-pyrophosphates **7** (Fig. 2) that were reacted with (*S*)-HPMPFU or (*S*)-HPMPC to give β-cyanoethyl-alkyl-triphosphate analogues of the nucleoside phosphonates **8** (Fig. 2).

2.3. γ-Undecanoyl-(S)-HPMPFU-diphosphate 11a

Step A: 100 mg (346 μmol, 1.00 equiv.) (β-cyanoethyl)-undecanoyl-*H*-phosphonate **6,** 92.3 mg (691 μmol, 2.00 equiv.) *N*-chlorosuccinimide in dry CH_3CN, 2.16 mL (864 μmol, 2.50 equiv.) tetra-*n*-butylammonium phosphate solution (0.4 M in CH_3CN), yield: 178 mg (284 μmol, 82%) of a colorless oil.
Step B: 178 mg (284 μmol, 1.00 equiv.) (β-cyanoethyl)-undecanoyl-pyrophosphate **7** in dry CH_3CN, 570 μL (4.15 mmol, 12.0 equiv.) NEt_3, 490 μL (3.46 mmol, 10.0 equiv.) trifluoroacetic acid anhydride, 570 μL (4.13 mmol, 12.0 equiv.) NEt_3, 170 μL (2.07 mmol, 6.00 equiv.) methylimidazol, 89.8 mg (136 μmol, 0.50 equiv.) *(S)*-HPMPFU as tetrabutylammonium salt, 200 μL (1.36 mmol, 20 equiv.) TBAH; yield: 27.6 mg (41.6 μmol, 31%) of a colorless cotton.

UV (HPLC): $\lambda_{max} = 275$ nm. HPLC (method A): $t_r = 11.24$ min (98% purity). ^{1}H-NMR (600 MHz, CD_3OD): δ [ppm]: 8.01 (d, $^3J_{H,F} = 6.4$ Hz, 1H, H-6), 4.01 – 3.93 (m, 4H, H-a, H-4′), 3.89 (dd, $^1J_{H,H} = 14.3$, $^3J_{H,H} = 7.0$ Hz, 1H, H-1′a), 3.85 – 3.78 (m, 2H, H-1′b, H-3′a), 3.69 (dq, $^3J_{H,H} = 7.7$, 3.9 Hz, 1H, H-2′), 3.51 (dd, $^1J_{H,H} = 12.6$, $^3J_{H,H} = 4.1$ Hz, 1H, H-3′b), 1.72 – 1.59 (m, 2H, H-b), 1.38 (q, $^3J_{H,H} = 7.1$ Hz, 2H, H-c), 1.36 – 1.25 (m, 14H, H-d, H-e, H-f, H-g, H-h, H-I, H-j), 0.90 (t, $^3J_{H,H} = 7.0$ Hz, 3H, H-k). ^{31}P-NMR (162 MHz, CD_3OD): δ [ppm]: 7.52 (d, $^2J_{P,P} = 23.9$ Hz, P-α), −10.77 (d, $^2J_{P,P} = 19.1$ Hz, P-γ), −22.48 (dd, $^2J_{P,P} = 24.6$, 19.4 Hz, P-β). ^{19}F-NMR (565 MHz, CD_3OD): δ [ppm]: −170.80 (d, $^3J_{H,F} = 6.3$ Hz). ^{13}C-NMR (151 MHz, CD_3OD): δ [ppm]: 160.02 (d, $^3J_{C,F} = 25.5$ Hz, C-4), 151.84 (C-2), 141.41 (d, J = 231.1 Hz, C-5), 132.72 (d, $^3J_{C,F} = 33.6$ Hz, H-6), 81.66 (d, $^3J_{C,P} = 12.1$ Hz, H-2′), 67.47 (d, $^1J_{C,P} = 164.0$ Hz, C-4′), 67.38 (d, $^2J_{C,P} = 6.4$ Hz, C-a), 61.55 (C-3′), 50.09 (C-1′), 33.08, 31.82 (d, $^3J_{C,P} = 8.2$ Hz, C-b), 30.89 – 30.38 (m), 26.91, 23.74 (C-c, C-d, C-e, C-f, C-g, C-h, C-I, C-j), 14.43 (C-k). HRMS (ESI-MS): m/z = calc.: 611.1342 [M+2H], found: 611.1500.

2.4. γ-Octadecanoyl-(S)-HPMPFU-diphosphate 11b

Step A: 150 mg (387 μmol, 1.00 equiv.) (β-cyanoethyl) octadecanoyl-*H*-phosphonate **6,** 106 mg (774 μmol, 2.00 equiv.) *N*-chlorosuccinimide in dry CH_3CN, 2.42 mL (968 μmol, 2.50 equiv.) tetra-*n*-butylammonium phosphate solution (0.4 M in CH_3CN), yield: 207 mg (286 μmol, 66%) of a colorless oil.
Step B: 207 mg (286 μmol, 1.00 equiv.) (β-cyanoethyl)-octadecanoyl-pyrophosphate **7** in dry CH_3CN, 640 μL (4.65 mmol, 12.0 equiv.) NEt_3, 550 μL (3.87 mmol, 10.0 equiv.) trifluoroacetic acid anhydride, 640 μL (4.65 mmol, 12.0 equiv.) NEt_3, 190 μL (2.32 mmol, 6.00 equiv.) methylimidazol, 90.6 mg (137 μmol, 0.500 equiv.) *(S)*-HPMPFU as tetrabutylammonium salt, 200 μL (1.36 mmol, 20.0 equiv.) TBAH; yield: 13.5 mg (17.7 μmol, 13%) of a colorless cotton.

UV (HPLC): $\lambda_{max} = 275$ nm. HPLC (method A): $t_r = 13.53$ min (98% purity). ^{1}H-NMR (600 MHz, CD_3OD): δ [ppm]: 8.01 (d, $^3J_{H,F} = 6.4$ Hz, 1H, H-6), 4.01 – 3.93 (m, 6H, H-a, H-4′), 3.92 – 3.84 (m, 1H, H-3′a), 3.84 – 3.79 (m, 2H, H-3′b, H-1′a), 3.72 – 3.67 (m, 1H, H-2′), 3.50 (dd, $^1J_{H,H} = 12.6$, $^3J_{H,H}$ 4.2 Hz, 1H, H-1′b), 1.64 (p, $^3J_{H,H} = 6.8$ Hz, 2H, H-b), 1.39 (t, $^3J_{H,H} = 7.1$ Hz, 2H, H-c), 1.34 – 1.18 (m, 28H, H-d, H-e, H-f, H-g, H-h, H-i, H-j, H-k, H-l, H-m, H-n, H-o, H-p, H-q), 0.89 (t, $^3J_{H,H} = 7.0$ Hz, 3H, H-r). ^{31}P-NMR (243 MHz, CD_3OD): δ [ppm]: 7.58 (d, $^2J_{P,P} = 24.7$ Hz, P-α), −10.93 (d, $^2J_{P,P} = 20.3$ Hz, P-γ), −22.86 (pseudo t, $^2J_{P,P} = 22.0$ Hz, P-β). ^{19}F-NMR (565 MHz, CD_3OD): δ [ppm]: −170.88 (d, $^3J_{F,H} = 6.8$ Hz). ^{13}C-NMR (151 MHz, CD_3OD): δ [ppm]: 159.93 (d, $^2J_{C,F} = 25.9$ Hz, C-4), 151.76 (C-2), 141.23 (d $^1J_{C,F} = 231.0$ Hz, C-5), 132.74 (d, $^2J_{C,F} = 33.6$ Hz, C-6), 81.71 (d, $^3J_{C,P} = 12.0$ Hz. C-2′), 67.50 (d, $^1J_{C,P} = 163.8$ Hz, C-4′), 61.64 (C-3′), 67.38 (d, $^2J_{C,P} = 6.4$ Hz, C-a), 50.08 (C-1′), 33.08, 31.24 (d, $^3J_{C,P} = 7.3$ Hz, C-b), 30.97 – 30.60 (m), 30.48, 30.31, 28.08, 26.56, 24.78 (C-c, C-d, C-e, C-f, C-g, C-h, C-I, C-j, C-k, C-l, C-m, C-n, C-o, C-p, C-q),14.09 (C-r). HRMS (ESI-MS): m/z = calc.: 709.2437 [M+2H]-, found: 709.2505.

2.5. γ-Undecanoyl-(S)-HPMPC-diphosphate 12[a]

Step A: 108 mg (373 μmol, 1.00 equiv.) (β-cyanoethyl)-undecanoyl-*H*-phosphonate **6,** 99.7 mg (746 μmol, 2.00 equiv.) *N*-chlorosuccinimide in dry CH_3CN, 2.33 mL (93.3 μmol, 2.50 equiv.) tetra-*n*-butylammonium phosphate solution (0.4 M in CH_3CN), yield: 184 mg (294 μmol, 79%) of a colorless oil.
Step B: 184 mg (294 μmol, 1.00 equiv.) (β-cyanoethyl)-undecanoyl-pyrophosphate **7** in dry CH_3CN, 640 μL (4.65 mmol, 12.0 equiv.) NEt_3, 620 μL (4.48 mmol, 12.0 equiv.) trifluoroacetic acid anhydride, 620 μL (4.48 mmol, 12.0 equiv.) NEt_3, 180 μL (2.34 mmol, 6.00 equiv.) methylimidazol, 87.1 mg (147 μmol, 0.50 equiv.) *(S)*-HPMPC as tetrabutylammonium salt, 200 μL (1.36 mmol, 20.0 equiv.) TBAH; yield: 40.5 mg (62.8 μmol, 48%) of a colorless cotton.

UV (HPLC): $\lambda_{max} = 275$ nm. HPLC (method A): $t_r = 11.06$ min (95% purity). ^{1}H-NMR (600 MHz, CD_3OD): δ [ppm]: 7.94 (d, $^3J_{H,H} = 7.6$ Hz, 1H, H-6), 6.11 (d, $^3J_{H,H} = 7.5$ Hz, 1H, H-5), 4.19 – 4.14 (m, 1H, H-1′a), 4.04 – 3.95 (m, 4H, H-a, H-4′), 3.92 – 3.73 (m, 3H, H-3′a, H-2′, H-3′b), 3.57 – 3.50 (m, 1H, H-1′b), 1.65 (p, $^3J_{H,H} = 6.7$ Hz, 2H, H-b), 1.43 – 1.36 (m, 2H, H-c), 1.36 – 1.24 (m, 14H, H-d, H-e, H-f, H-g, H-h, H-i, H-j), 0.90 (t, $^3J_{H,H} = 7.0$ Hz, 3H, H-k). ^{31}P-NMR (243 MHz, CD_3OD): δ [ppm]: 7.65 (d, $^2J_{P,P} = 23.9$ Hz, P-α), −10.69 (d, $^2J^{P,P} = 18.0$. Hz, P-γ), −21.77 – 23.32 (m, P-β). ^{13}C-NMR (151 MHz, CD_3OD): δ [ppm]: 161.28 (C-2), 151.45 (C-6), 150.87 (C-4), 95.06 (C-5), 81.04 (C-2′), 67.41 (d, $^2J_{C,P} = 6.4$ Hz, C-a), 66.65 (d, $^1J_{C,P} = 160.7$ Hz, C-4′), 59.34 (C-1′), 50.90 (C-3′), 32.80, 31.56, 30.58 – 30.28 (m), 30.16, 26.67, 24.59, 23.52, 20.50 (C-b, C-c, C-d, C-f, C-g, C-h, C-I, C-j), 14.41 (C-k). HRMS (ESI-MS): m/z = calc.: 592.1596 [M+2H]-, found: 592.1500.

2.6. γ-Octadecanoyl-(S)-HPMPC-diphosphate 12b

Step A: 117 mg (303 μmol, 1.00 equiv.) (β-cyanoethyl)-octadecanoyl-*H*-phosphonate **6,** 82.6 mg (606 μmol, 2.00 equiv.) *N*-chlorosuccinimide in dry CH_3CN, 1.89 mL (757 μmol, 2.50 equiv.) tetra-*n*-butylammonium phosphate solution (0.4 M in CH_3CN), yield: 146 mg (201 μmol, 66%) of a colorless oil.
Step B: 146 mg (201 μmol, 1.00 equiv.) (β-cyanoethyl)-octadecanoyl-pyrophosphate **7** in dry CH_3CN, 500 μL (3.64 mmol, 12.0 equiv.) NEt_3, 430 μL (3.03 mmol, 10.0 equiv.) trifluoroacetic acid anhydride, 500 μL (3.64 mmol, 12.0 equiv.) NEt_3, 140 μL (1.82 mmol, 6.00 equiv.) methylimidazol, 90.2 mg (141 μmol, 0.50 equiv.) *(S)*-HPMPC as tetrabutylammonium salt, 200 μL (1.36 mmol, 20.0 equiv.) TBAH; yield: 49.3 mg (66.4 μmol, 47%) of a colorless cotton.

UV (HPLC): $\lambda_{max} = 275$ nm. HPLC (method A): $t_r = 13.38$ min (97% purity). ^{1}H-NMR (600 MHz, CD_3OD): δ [ppm]: 8.02 (d, $^3J_{H,H} = 7.6$ Hz, 1H, H-6), 6.18 (d, $^3J_{H,H} = 7.6$ Hz, 1H, H-5), 4.18 (dd, $^1J^{H,H} = 14.3$, $^3J_{H,H} = 2.9$ Hz, 1H, H-1′a), 3.98 (q, $^3J_{H,H} = 6.7$ Hz, 2H, H-a), 3.95 – 3.86 (m, 2H, H-4′), 3.82 (dd, $^1J_{H,H} = 12.6$, $^3J_{H,H} = 3.7$ Hz, 1H, H-3′a), 3.76 (dd, $^1J_{H,H} = 12.8$, $^3J_{H,H} = 9.9$ Hz, 1H, H-3′b), 3.71 (dq, $^3J_{H,H} = 7.4$, 3.7 Hz, 1H, H-2′), 3.55 (dd, $^1J_{H,H} = 12.6$, $^3J_{H,H} = 4.1$ Hz, 1H, H-1′b), 1.42 (p, $^3J_{H,H} = 7.4$ Hz, 2H, H-b), 1.26 (s, 30H, H-c, H-d, H-e, H-f, H-g, H-h, H-I, H-j, H-k, H-l, H-m, H-n, H-o, H-p, H-q), 0.88 (t, $^3J_{H,H} = 7.0$ Hz, 3H, H-r). ^{31}P-NMR (243 MHz, CD_3OD): δ [ppm]: 7.66 (d, $^2J_{P,P} = 24.8$ Hz, P-α), −10.98 (d, $^2J_{P,P} = 19.1$ Hz, P-γ), −23.14 (dd, $^2J_{P\ P,}$ = 24.6, 19.2 Hz, P-β). ^{13}C-NMR (151 MHz, CD_3OD): δ [ppm]:161.35 (C-2), 151.90 (C-6), 150.55 (C-4), 95.19 (C-5), 80.96 (C-2′), 67.59 (C-a), 66.91 (d, $^1J_{C,P} = 160.7$ Hz, C-4′), 59.34 (C-1′), 50.90 (C-3′), 32.80, 31.56, 30.58 – 30.28 (m), 30.16, 26.67, 24.59, 23.52, 20.50 (C-b, C-c, C-d, C-f, C-g, C-h, C-I, C-j, C-k, C-k, C-m, C-n, C-o, C-p, C-q), 14.41 (C-r). HRMS (ESI-MS): m/z = calc.: 690.2691 [M+2H]-, found: 690.2500.

2.7. Preparation of γ-alkyl-γ-acyloxybenzyl-TriPPPro-compounds 15 and 16

The compounds were prepared according to the general procedures given in ref (Kullik, 2023; Jia et al., 2024). using acyloxybenzyl-alkyl-*H*-phosphonates **9** (1.0 equiv.) pyrophosphates **10** (Fig. 2) and (*S*)-HPMPC or (*S*)-HPMPFU salts.

2.8. Ammonium-(4-pentanoyloxybenzyl)-octadecanoyl-(S)-HPMPC-diphosphate 15a

Amounts of reagents: step A: 210 mg (400 μmol, 1.00 equiv.) (4-pentanoyloxybenzyl)-octadecanoyl-phosphonate **9,** 107 mg (800 μmol, 2.00 equiv.) *N*-chlorosuccinimide in dry CH_3CN, 2.50 mL (1.00 mmol, 2.50 equiv.) tetra-*n*-butylammonium phosphate-solution (0.4 M in CH_3CN), yield**:** 342 mg (397 μmol, 99%) of a colorless oil.

Step B: 342 mg (397 μmol, 1.00 equiv.) (4-pentanoyloxybenzyl)-octadecanoyl-pyrophosphate **10** in dry CH_3CN, 660 μL (4.76 mmol, 12.0 equiv.) NEt_3, 560 μL (3.97 mmol, 10.0 equiv.) trifluoroacetic acid anhydride, 660 μL (4.76 mmol, 12.0 equiv.) NEt_3, 190 μL (2.38 mmol, 6.00 equiv.) methylimidazol, 122 mg (198 μmol, 0.50 equiv.) *(S)*-HPMPC as tetrabutylammonium salt; yield: 60.1 mg (65.6 μmol, 33% yield) as a colorless cotton.

UV (HPLC): $\lambda_{max} = 275$ nm. HPLC (method A): $t_r = 16.27$ min (96% purity). ^{1}H-NMR (600 MHz, CD_3OD): δ [ppm]: 7.90 (dd, $^3J_{H,H} = 7.5$, $^4J_{H,H} = 1.1$ Hz, 1H, H-6), 7.53 – 7.47 (m, 2H, H-C), 7.11 – 7.05 (m, 2H, H-B), 5.98 (d, $^3J_{H,H} = 7.5$ Hz, 1H, H-5), 5.21 (d, $^3J_{H,P} = 8.2$ Hz, 2H, H-E), 4.16 – 4.05 (m, 3H, H-4′, H-a), 3.91 (dd, $^1J_{H,H} = 12.8$, $^3J_{H,H} = 9.8$ Hz, 1H, H-1′a), 3.84 – 3.73 (m, 2H, H-3′a, H-3′b), 3.73 – 3.66 (m, 1H, H-2), 3.51 (dd, $^1J_{H,H} = 12.5$, $3J_{H,H} = 4.1$ Hz, 1H, H-1′b), 2.57 (t, $3J_{H,H} = 7.4$ Hz, 2H, H-b), 1.75 – 1.67 (m, 2H, H-c), 1.67 – 1.55 (m, 2H, H-b), 1.49 – 1.38 (m, 4H, H-d, H-c), 1.34 – 1.21 (m, 28H, H-d, H-e, H-f, H-g, H-h, H-I, H-j, H-k, H-l, H-m, H-n, H-o, H-p, H-q), 1.01 (t, $3J_{H,H} = 7.4$ Hz, 3H, H-r), 0.97 (t, $3J_{H,H} = 7.4$ Hz, 3H, H-e′). ^{31}P-NMR (243 MHz, CD_3OD): δ [ppm]: 7.34 (d, $2J_{P,P} = 25.8$ Hz, P-α), −13.08 (d, $2J_{P,P} = 17.4$ Hz, P-γ), −24.03 (dd, $2J_{P,P}$ = 25.4, 17.1 Hz, P-β). ^{13}C-NMR (151 MHz, CD_3OD): δ [ppm]: 173.93 (C-a′), 162.48 (C-2) 152.26 (C-6), 151.33 (C-4), 135.29 (d, $^3J_{C,P} = 7.4$ Hz, C-D), 130.44 (C-C), 130.35 (C-B), 129.10 (C-A), 95.04 (C-5), 81.37 (d, $^3J_{C,P} = 12.0$ Hz, C-2′), 70.27 (d, $^2J_{C,P} = 5.6$ Hz, C-E), 69.92 (d, $^2J_{C,P} = 6.2$ Hz, C-a), 67.21 (d, J = 164.5 Hz, C-4′), 61.54 (C-1′), 51.09 (C-3′), 34.78 (C-b′), 33.03, 31.20, 30.80 – 30.60 (m), 30.42, 30.27, 28.06 (C-c′), 26.53, 24.76, 23.71, 23.23 (C-b, C-c, C-d, C-e, C-f, C-g, C-h, C-i, C-j, C-k, C-l, C-m, C-n, C-o, C-p, C-q), 20.67 (C-d′), 14.11 (C-r), 13.95 (C-e′). HRMS (ESI-MS): m/z = calc.: 880.3685 [M+H]-, found: 880.3500.

2.9. Ammonium (4-nonanoyloxybenzyl)-octadecanoyl-(S)-HPMPC-diphosphate 15b

Amounts of reagents: step A: 210 mg (362 μmol, 1.00 equiv.) (4-nonanoyloxybenzyl)-octadecanoyl-*H*-phosphonate **9,** 96.6 mg (723 μmol, 2.00 equiv.) *N*-chlorosuccinimide in dry CH_3CN, 2.26 mL (90.4 μmol, 2.50 equiv.) tetra-*n*-butylammonium phosphate solution (0.4 M in CH_3CN); yield: 256 mg (279 μmol, 77%) of a colorless oil.

Step B: 256 mg (279 μmol, 1.00 equiv.) (4-nonanoyloxybenzyl)-octadecanoyl-pyrophosphate **10** in dry CH_3CN, 460 μL (3.53 mmol, 12.0 equiv.) NEt_3, 390 μL (2.79 mmol, 10.0 equiv.) trifluoroacetic acid anhydride, 460 μL (3.53 mmol, 12.0 equiv.) NEt_3, 130 μL (1.68 mmol, 6.00 equiv.) methylimidazol, 89.5 mg (140 μmol, 0.50 equiv.) *(S)*-HPMPC as tetrabutylammonium salt; yield: 31.7 mg (32.6 μmol, 23%) as a colorless cotton.

UV (HPLC): $\lambda_{max} = 275$ nm. HPLC (method A): $t_r = 17.78$ min (97% purity). ^{1}H-NMR (600 MHz, CD_3OD): δ [ppm]: 7.95 (dd, $^3J_{H,H}$ = 7.6,

3.1 Hz, 1H, H-6), 7.52 – 7.47 (m, 2H, H-C), 7.09 – 7.04 (m, 2H, H-B), 6.01 (dd, $^{3}J_{H,H}$ = 7.6, 2.1 Hz, 1H, H-5), 5.21 (d, $^{3}J_{H,P}$ = 8.5 Hz, 2H, H-E), 4.25 – 4.15 (m, 1H, H-1′a), 4.14 – 4.06 (m, 2H, H-a), 3.97 – 3.89 (m, 1H, H-3′a), 3.86 – 3.72 (m, 4H, H-4′, H-2′, H-3′b), 3.55 – 3.48 (m, 1H, H-1′b), 2.56 (t, $^{3}J_{H,H}$ = 7.4 Hz, 2H, H-b′), 1.76 – 1.68 (m, 2H, H-c′), 1.60 (q, $^{3}J_{H,H}$ = 7.2 Hz, 2H, H-b), 1.45 – 1.23 (m, 40H, H-c, H-d, H-e, H-f, H-g, H-h, H-I, H-j, H-k, H-l, H-m, H-n, H-o, H-p, H-q, H-d′, H-e′, H-f′, H-g′, H-h′), 0.90 (pseudo q, $^{3}J_{H,H}$ = 7.1 Hz, 6H, H-r, H-i′). ^{31}P-NMR (243 MHz, CD_3OD): δ [ppm]: 7.36 (dd, $^{2}J_{P,P}$ = 21.2, 5.0 Hz, P-α), −13.06 (dd, $^{2}J_{P,P}$ = 17.4, 7.4 Hz, P-γ), −23.97 (ddd, $^{2}J_{P,P}$ = 23.9, 17.0, 5.6 Hz, P-β). ^{13}C-NMR (151 MHz, CD_3OD): δ [ppm]: 173.66 (C-a), 152.32 (C-6), 130.38 (C-C), 122.85 (C-B), 122.83, 122.81, 94.53 (C-5), 80.84 (C-2′), 70.24 (d, $^{2}J_{C,P}$ = 6.1 Hz, C-a), 69.85 (d, $^{2}J_{C,P}$ = 6.4 Hz, H-E), 66.81 (d, $^{1}J_{C,P}$ = 219.4 Hz, C-4′), 61.45 (C-1′), 51.31 (C-3′), 49.57, 35.06 (C-b), 33.05, 31.25, 31.04 – 30.62 (m), 30.49, 30.41, 30.32, 30.21, 26.57, 25.99, 24.78, 23.75, 23.73 (C-b, C-c, C-d, C-e, C-g, C-h, C-I, C-j, C-k, C-l, C-m, C-n, C-o, C-p, C-q, c-c′, C-d′, C-e′, C-g′, C-h′), 14.46 (C-r, C-i′). HRMS (ESI-MS): m/z = calc.: 936.4311 [M+H]-, found: 936.3990.

2.10. Ammonium (4-pentanoyloxybenzyl)-octadecanoyl-(S)-HPMPFU-diphosphate 16[a]

Step A: 170 mg (324 μmol, 1.00 equiv.) (4-pentanoyloxybenzyl)-octadecanoyl-phosphonate **9,** 86.5 mg (648 μmol, 2.00 equiv.) *N*-chlorosuccinimide in dry CH_3CN, 2.02 mL (810 μmol, 2.50 equiv.) tetra-*n*-butylammonium phosphate solution (0.4 M in CH_3CN), yield: 241 mg (280 μmol, 87%) of a colorless oil.

Step B: 241 mg (280 μmol, 1.00 equiv.) (4-pentanoyloxybenzyl)-octadecanoyl-pyrophosphate **10** in dry CH_3CN, 470 μL (3.36 mmol, 12.0 equiv.) NEt_3, 400 μL (2.80 mmol, 10.0 equiv.) trifluoroacetic acid anhydride, 470 μL (3.36 mmol, 12.0 equiv.) NEt_3, 130 μL (1.68 mmol, 6.00 equiv.) methylimidazol, 92.5 mg (140 μmol, 0.50 equiv.) *(S)*-HPMPFU as tetrabutylammonium salt; yield: 39.4 mg (42.1 μmol, 30%) as a colorless cotton.

UV (HPLC): λ_{max} = 275 nm. HPLC (method A): t_r = 16.36 min (96% purity). ^{1}H-NMR (600 MHz, CD_3OD): δ [ppm]: 8.00 (d, $^{3}J_{H,F}$ = 6.3 Hz, 1H, H-6), 7.52 – 7.48 (m, 2H, H-C), 7.11 – 7.06 (m, 2H, H-B), 5.22 (d, $^{3}J_{H,P}$ = 8.0 Hz, 2H, H-E), 4.18 – 4.09 (m, 2H, H-a), 3.98 – 3.91 (m, 2H, H-4′), 3.90 – 3.82 (m, 2H, H-1′), 3.82 – 3.77 (m, 1H, H-3′a), 3.71 – 3.65 (m, 1H, H-2′), 3.53 – 3.46 (m, 1H. H-3′b),2.58 (t, $^{3}J_{H,H}$ = 7.4 Hz, 2H, H-b′), 2.58 (t, $^{3}J_{H,H}$ = 7.4 Hz, 2H, H-b′), 1.72 (p, J = 7.2 Hz, 2H, H-c′), 1.68 – 1.58 (m, 2H, H-b), 1.50 – 1.37 (m, 2H, H-d′), 1.36 – 1.22 (m, 30H, H-c, H-d, H-e, H-f, H-g, H-h, H-i, H-j, H-k, H-l, H-m, H-n, H-o, H-p, H-q), 0.99 (t, $^{3}J_{H,H}$ = 7.4 Hz, 3H, H-e′), 0.90 (t, $^{3}J_{H,H}$ = 7.0 Hz, 3H, H-r). ^{31}P-NMR (162 MHz, CD_3OD): δ [ppm]: 7.43 (d, $^{2}J_{P,P}$ = 24.9 Hz, P-α), −13.04 (d, $^{2}J_{P,P}$ = 17.1 Hz, P-γ), −23.74 (dd, $^{2}J_{P,P}$ = 24.5, 17.0 Hz, P-β). ^{19}F-NMR (565 MHz, CD_3OD): δ [ppm]: −170.73 (d, $^{3}J_{H,F}$ = 6.7 Hz). ^{13}C-NMR (151 MHz, CD_3OD): δ [ppm]: 173.75 (C-a′), 159.93 (d, $^{2}J_{C,F}$ = 25.9 Hz, C-4), 152.35 (C-A), 151.76 (C-2), 141.23 (d 1JC,F = 231.0 Hz, C-5), 135.02 (d, $^{3}J_{C,P}$ = 7.3 Hz, C-D), 132.74 (d, $^{2}J_{C,F}$ = 33.6 Hz, C-6), 130.50 (C-C), 122.85 (C-B), 81.71 (d, $^{3}J_{C,P}$ = 12.0 Hz. C-2′), 70.38 (d, $^{3}J_{C,P}$ = 5.8 Hz, C-E), 67.50 (d, $^{1}J_{C,P}$ = 163.8 Hz, C-4′), 61.64 (C-3′), 50.08 (C-1′), 34.77 (C-b′), 33.08, 31.24 (d, $^{3}J_{C,P}$ = 7.3 Hz, C-b), 30.97 – 30.60 (m), 30.48, 30.31, 28.08 (C-c′), 26.56, 24.78 (C-c, C-d, C-e, C-f, C-g, C-h, C-I, C-j, C-k, C-l, C-m, C-n, C-o, C-p, C-q), 23.50 (C-d′), 14.44 (C-e′), 14.09 (C-r). HRMS (ESI-MS): m/z = calc.: 899.3431 [M+H]-, found.: 899.3410.

2.11. Ammonium (4-nonanoyloxybenzyl)-octadecanoyl-(S)-HPMPFU-diphosphate 16b

Step A: 210 mg (362 μmol, 1.00 equiv.) (4-nonanoyloxybenzyl)-octadecanoyl-phosphonate **9,** 96.6 mg (723 μmol, 2.00 equiv.) *N*-chlorosuccinimide in dry CH_3CN, 2.26 mL (90.4 μmol, 2.50 equiv.) tetra-*n*-butylammonium phosphate solution (0.4 M in CH_3CN), yield: 315 mg (344 μmol, 95%) of a colorless oil.

Step B: 315 mg (344 μmol, 1.00 equiv.) (4-nonanoyloxybenzyl)-octadecanoyl-pyrophosphate **10** in dry CH_3CN, 570 μL (4.13 mmol, 12.0 equiv.) NEt_3, 480 μL (3.44 mmol, 10.0 equiv.) trifluoroacetic acid anhydride, 570 μL (4.13 mmol, 12.0 equiv.) NEt_3, 160 μL (2.06 mmol, 6.00 equiv.) methylimidazol, 134 mg (172 μmol, 0.50 equiv.) *(S)*-HPMPFU as tetrabutylammonium salt; yield: 9.90 mg (10.0 μmol, 6%) as a colorless cotton.

UV (HPLC): λ_{max} = 275 nm. HPLC (method A): t_r = 18.71 min (95% purity). ^{1}H-NMR (600 MHz, CD_3OD): δ [ppm]: 8.00 (d, $^{3}J_{H,F}$ = 6.3 Hz, 1H, H-6), 7.52 – 7.48 (m, 2H, H-C), 7.11 – 7.06 (m, 2H, H-B), 5.22 (d, $^{3}J_{H,P}$ = 8.0 Hz, 2H, H-E), 4.18 – 4.09 (m, 2H, H-a), 3.98 – 3.91 (m, 2H, H-4′), 3.90 – 3.82 (m, 2H, H-1′), 3.82 – 3.77 (m, 1H, H-3′a), 3.71 – 3.65 (m, 1H, H-2′), 3.53 – 3.46 (m, 1H. H-3′b), 2.58 (t, $^{3}J_{H,H}$ = 7.4 Hz, 2H, H-b′), 1.72 (p, $^{3}J_{H,H}$ = 7.5 Hz, 2H, H-b), 1.67 – 1.51 (m, 2H, H-c), 1.39 – 1.22 (m, 40H, H-c, H-d, H-e, H-f, H-g, H-h, H-i, H-j, H-k, H-l, H-m, H-n, H-o, H-p, H-q, H-d′, H-e′, H-f′, H-g′, H-h′), 0.90 (q, $^{3}J_{H,H}$ = 7.1 Hz, 6H, H-r, H-i′). ^{31}P-NMR (162 MHz, CD_3OD): δ [ppm]: 7.51 (d, $^{2}J_{P,P}$ = 25.1 Hz, P-α), −13.04 (d, $^{2}J_{P,P}$ = 17.1 Hz, P-γ), −23.85 (dd, $^{2}J_{P,P}$ = 25.7, 17.3 Hz, P-β). ^{19}F-NMR (565 MHz, CD_3OD): δ [ppm]: −170.73 (d, $^{3}J_{H,F}$ = 6.2 Hz). ^{13}C-NMR (151 MHz, CD_3OD): δ [ppm]: 173.75 (C-a′), 159.93 (d, $^{2}J_{C,F}$ = 25.9 Hz, C-4), 152.35 (C-A), 151.76 (C-2), 141.23 (d $^{1}J_{C,F}$ = 231.0 Hz, C-5), 135.02 (d, $^{3}J_{C,P}$ = 7.3 Hz, C-D), 132.74 (d, $^{2}J_{C,F}$ = 33.6 Hz, C-6), 130.50 (C-C), 122.85 (C-B), 81.71 (d, $^{3}J_{C,P}$ = 12.0 Hz. C-2′), 70.38 (d, $^{3}J_{C,P}$ = 5.8 Hz, C-E), 67.50 (d, $^{1}J_{C,P}$ = 163.8 Hz, C-4′), 61.64 (C-3′), 50.08 (C-1′), 34.77 (C-b′), 33.08, 31.24 (d, $^{3}J_{C,P}$ = 7.3 Hz, C-b), 30.97 – 30.60 (m), 30.48, 30.31, 28.08, 26.56, 24.78 (C-c, C-d, C-e, C-f, C-g, C-h, C-I, C-j, C-k, C-l, C-m, C-n, C-o, C-p, C-q, C-c′, C-d′, C-e′, C-f′, C-g′, C-h′), 23.50 (C-d′), 14.44 (C-e′), 14.09 (C-r). HRMS (ESI-MS): m/z = calc.: 955.4057 [M+H]-, found: 955.4000.

2.12. Dibenzyl octadecyl-1-phosphate

A solution of 500 mg 1-octadecanol (1.85 mmol, 1.0 equiv.) and 930 μL dibenzyl-*N*,*N*-diisopropylphosphoramidite (960 mg, 2.77 mmol, 1.5 equiv.) in dry CH_2Cl_2 was treated with 14.8 mL of a 0.25 M solution of 4,5-dicyanoimidazole in CH_3CN (3.70 mmol, 2.0 equiv.) and stirred at room temperature. After 4h 480 mg 3-chloroperoxybenzoic acid (2.77 mmol, 1.5 equiv.) was added in portions and the mixture was stirred for 1h at 0°C. The solution was washed with sat. $NaHCO_3$ solution, dried over Na_2SO_4 and concentrated in vacuo. The residue was purified by column chromatography on silica gel (petroleum ether/EtOAc 6:1 → 4:1).

Yield: 977 mg (1.84 mmol, quant.) of a colorless oil. R_f = 0.31 (petroleum ether/EtOAc 4:1). ^{1}H-NMR: *δ* [ppm] (400 MHz, $CDCl_3$): 7.39 – 7.28 (m, 10 H, H-3, H-4, H-5), 5.05 (m, 2 H, H-1), 3.99 (q, $^{3}J_{H-H}$ = 6.7 Hz, 2 H, H-a), 1.61 (m, 2 H, H-b), 1.38 – 1.14 (m, 30 H, H-c – H-q), 0.88 (t, $^{3}J_{H-H}$ = 6.7 Hz, 3 H, H-r). ^{13}C-NMR: *δ* [ppm] (101 MHz, $CDCl_3$): 136.1 (C-2), 128.6 (C-4), 128.5 (C-5), 128.0 (C-3), 69.2 (C-1), 68.2 (C-a), 30.2 (C-b), 32.0, 29.8, 29.8, 29.8, 29.7, 29.7, 29.6, 29.5, 29.2 (C-c – C-q), 14.2 (C-r). ^{31}P-NMR: *δ* [ppm] (122 MHz, $CDCl_3$): − 0.75. HRMS (ESI-MS): m/z = calc.: 531.3598 $[M+H]^+$, found: 531.3600 $[M+H]^+$.

2.13. Octadecyl-1-phosphate

A solution of 800 mg dibenzyl octadecyl-1-phosphate (1.51 mmol, 1.0 equiv.) in ethanol/water (10:1, v/v) was treaded with 420 μL triethylamine (300 mg, 3.01 mmol, 2.0 equiv.) and 160 mg Pd(OH)2/C (20 wt%). The reaction flask was purged three times with nitrogen and three times with hydrogen. The suspension was stirred under hydrogen atmosphere for 16h, filtered over Celite® and washed with methanol. The filtrate was concentrated in vacuo.

Yield: 672 mg (1.53 mmol, quant.) of a colorless solid. 1H NMR: δ [ppm] (400 MHz, CDCl3): 3.90 (q, 3JH H = 6.6 Hz, 2 H, H a), 3.09 (q, 3JH H = 7.3 Hz, -CH2-), 1.61 (m, 2 H, H b), 1.35 (t, 3JH H = 7.3 Hz,

-CH3), 1.30 – 1.19 (m, 30 H, H c – H q), 0.86 (t, 3JH H = 6.8 Hz, 3 H, H r). 13C NMR: δ [ppm] (101 MHz, CDCl3): 66.0 (C a), 48.8 (CH2), 30.8 (C b), 32.1, 30.8, 29.9, 29.9, 29.8, 29.8, 29.6, 29.5, 25.9, 22.8 (C c – C q), 14.3 (C r), 8.7 (-CH3). 31P NMR: δ [ppm] (122 MHz, CDCl3): 1.47. HRMS (ESI-MS): m/z = calc.: 349.2513 [M H]-, found: 349.2556 [M-H]-.

The 1-octadecanol was purchased from TCI Deutschland GmbH.

2.14. Hydrolysis studies

The chemical in phosphate buffer saline, pH 7.3 and enzymatic stability in cell extracts of the CME-compounds were studied as described before (Jia et al., 2024).

2.15. Expression and purification of SARS-CoV-2 recombinant proteins

The SARS-CoV-2 nsp12/7/8 (RTC) complex was co-expressed in the *E. coli* BL21-Gold (DE3) strain using plasmid pRSFDuet-1 (nsp8-nsp7) (nsp12) (Addgene #165451), following a previously reported protocol (Madru et al., 2021), with minimal modifications. Recombinant SARS-CoV-2 nsp12, nsp7, and nsp8 were co-expressed in LB medium with 0.05 mM IPTG at 20°C for 18 h in 135 rpm agitation. After centrifugation, bacterial pellets were resuspended in a buffer containing 50 mM Tris-HCl pH 8.0, 500 mM NaCl, and 10 mM imidazole, supplemented with EDTA-free protease inhibitor cocktail (cOmplete Mini, Roche). Cells were lysed by ultrasonication, and the lysate was centrifuged at 16,000 rpm and 4°C for 45 min. The resulting supernatant was loaded into a HisTrap HP 5 mL column (Cytiva). The column was washed with 25 mL of lysis buffer, and protein was eluted using a gradient of elution buffer (50 mM Tris-HCl pH 8.0, 500 mM NaCl, and 500 mM imidazole). The presence of proteins in selected fractions was confirmed by SDS-PAGE, after which fractions were diluted tenfold with 50 mM Tris-HCl pH 8.0 and loaded onto a HiTrap Q HP 5 mL column (Cytiva). Proteins were eluted with a gradient of elute buffer (50 mM Tris-HCl pH 8.0 and 1 M NaCl). Selected fractions after SDS-PAGE were pooled, concentrated and further purified by size-exclusion chromatography (HiLoad 16/600 Superdex 200 pg column, Cytiva) in a buffer containing 50 mM Tris-HCl pH 8.0, 300 mM NaCl, and 1 mM $MgCl_2$ (Supplementary Fig. S2B). Protein purity was confirmed by SDS-PAGE (Supplementary Fig. S2A), after which fractions were pooled, concentrated and flash-frozen in liquid nitrogen and stored at −80°C.

The SARS-CoV-2 nsp12, nsp7 and nsp8 were expressed in the *E. coli* BL21 (DE3)-Gold strain using pET28 plasmids. Briefly, recombinant proteins were separately expressed in LB medium and induced with 0.4 mM IPTG at 20°C for 18 h in 135 rpm agitation. After centrifugation, bacterial pellets were resuspended in a buffer A (20 mM Tris-HCl pH 8.0, 500 mM NaCl, 5% glycerol, 10 mM imidazole, 1 mM DTT, 4 mM $MgCl_2$ for nsp12; and 20 mM Tris-HCl pH 7.5, 250 mM NaCl, 5% glycerol, 10 mM imidazole, 5 mM β-mercaptoethanol, 4 mM $MgCl_2$ for nsp7 and nsp8), supplemented with EDTA-free protease inhibitor cocktail (cOmplete Mini, Roche). Cells were lysed by ultrasonication, and the lysate was clarified by centrifugation at 16,000 rpm and 4°C for 45 min. Supernatant was loaded onto HisTrap HP 5 mL column (Cytiva). Column was washed with 25 mL of buffer A, then washed with 25 ml buffer A supplemented with 60 mM imidazole. The protein was eluted with the addition of 25 ml of elution buffer (buffer A with 300 mM imidazole). Elution fractions were pooled together, TEV protease was added, and protein was dialyzed at 4°C overnight against lysis buffer. The next day, the protein was centrifuged and loaded onto HisTrap HP 5 mL column. Column was washed with 25 mL of lysis buffer and bound proteins were eluted with 25 ml of elution buffer, as before. Flow-through fractions containing TEV-cleaved protein were concentrated and injected onto HiLoad 16/600 Superdex200 pg column (Cytiva) equilibrated with SEC buffer (50 mM HEPES pH 7.0, 100 mM NaCl for nsp12; and 20 mM Tris-HCl pH 7.5, 250 mM NaCl, 4 mM $MgCl_2$, 1 mM DTT for nsp17 and nsp8). Protein purity was confirmed by SDS-PAGE, then fractions containing pure recombinant protein were pooled together; the protein was concentrated and frozen in liquid nitrogen.

2.16. SARS-CoV-2 RdRp enzymatic assay

The RdRp activity of SARS-CoV-2 nsp12 and nsp7/8 complex was assessed by a primer-extension assay on denaturing urea-PAGE, similarly to a previously reported protocol(Lu et al., 2020). Briefly, an RNA template (28 nt, 3′-UCUUGGACAACUUGUUUUCGCGUACGAU-5′) was annealed with a Cy5-labelled RNA primer (20 nt, Cy5-5′-AGAACCUGUUGAACAAAAGC-3′) in a 1:1 ratio in 50 mM Tris-HCl pH 8.0 and 150 mM NaCl at a final concentration of 10 μM. The annealing mixture was denatured at 95°C for 10 min, then gradually cooled to 4°C overnight. SARS-CoV-2 co-purified RTC was pre-incubated at a final concentration of 150 nM in 5% DMSO in presence of serially diluted compounds at 37°C for 30 min in reaction buffer (20 mM HEPES pH 8.0, 25 mM NaCl, 1 mM $MgCl_2$, 10 mM DTT, 0.01% Tween 20, 5 nM RNA template, RNAse inhibitor [Euroclone]). Reactions were initiated by adding 1 μM rNTPs -for the incorporation check- or 20 μM rNTPs -for the dose-dependence evaluation-, followed by incubation at 37°C for 45 min. Then, 40 μL of stopping buffer (formamide with 4% EDTA) was added to each reaction. The reactions were denatured at 95°C for 10 min and resolved by 15% urea-PAGE (7 M urea, 19:1 acrylamide/bis-acrylamide in 1X TBE). Gels were scanned using a ChemiDoc Imager (Bio-Rad), and images were analyzed via densitometry using Image Lab 4.0 to quantify elongated vs non-elongated primer bands. The curve of enzymatic activity over reaction time was generated with GraphPad Prism 10.1. Eight points dose-response curves were generated with GraphPad Prism 10.1 by fitting the log10 inhibitor concentration against the normalized response using a variable-slope, non-linear regression. Suramin was used as internal positive control (Yin et al., 2021). Experiments were repeated in triplicate.

2.17. West Nile RdRp enzymatic assay

The RdRp activity of West Nile (WNV) NS5 was assessed by a primer-extension assay on denaturing urea-PAGE, similarly to the previously reported assay for SARS-CoV-2. Briefly, WNV NS5 was pre-incubated at a final concentration of 300 nM in 5% DMSO in presence of serially diluted compounds at 4°C for 30 min in reaction buffer (20 mM HEPES pH 8.0, 15 mM NaCl, 1 mM $MnCl_2$, 10 mM DTT, 0.01% Tween 20, 5 nM RNA template, RNAse inhibitor [Euroclone]). Reactions were initiated by adding 100 μM rNTPs followed by incubation at 37°C for 45 min. Then, 40 μL of stopping buffer (formamide with 4% EDTA) was added to each reaction. The reactions were denatured at 95°C for 10 min and resolved by 15% urea-PAGE (7 M urea, 19:1 acrylamide/bis-acrylamide in 1X TBE). Gels were scanned using a ChemiDoc Imager (Bio-Rad), and images were analyzed via densitometry using Image Lab 4.0 to quantify elongated vs non-elongated primer bands. Experiments were repeated in triplicate.

2.18. SARS-CoV-2 RdRp competition assay

Apparent Michaelis-Menten constant (K_M) of GTP and RNA substrate was assessed in the assay conditions reported above, in absence and in presence of different concentrations of inhibitor. Initial velocity was calculated by dividing enzymatic activity to pre-saturation steady state reaction time for each reaction. Initial velocity vs substrate concentration was plotted using GraphPad 10.1 with a non-linear regression using the Michaelis-Menten plot for apparent K_M determination (Johnson and Goody, 2011). Lineweaver-Burk plot was generated by calculating and plotting with linear regression on GraphPad Prism 10.1 the reciprocal of the initial velocities and substrate concentrations(Lineweaver and Burk, 1934).

2.19. Fluorescence polarization assay

Fluorescence polarization (FP) assay was conducted in reaction mix (20 mM HEPES pH 8.0, 25 mM NaCl, 1 mM $MgCl_2$, 10 mM DTT, 0.01% v/v Tween20, 62.5 nM Cy5-labelled primer/template RNA duplex, RNAse inhibitor [Euroclone]) in a black 384-multiwell (PerkinElmer). Serial 2-fold dilutions of SARS-CoV-2 co-purified RTC in SEC buffer were added to the wells containing the reaction mix and the compound at a concentration 10-fold higher than its IC_{50} value, or an equivalent amount of compound solvent for the negative control. The plate was incubated at 25°C for 30 min, after which Victor Nivo (PerkinElmer) was used to read FP signal with exc/em filters of 615/665 nm. Polarization values (expressed in mP) were calculated by the Victor Nivo software. Binding curves were generated using GraphPad Prism 10.1 and K_D values were obtained using the built-in "One-site - Specific binding" equation of non-linear regression for N = 3 replicates.

2.20. Native PAGE

Native PAGE was performed using the NativePAGE™ Novex® Bis-Tris Gel System (Life Technologies), following the manufacturer's instructions. Briefly, ~1.0 μg of nsp12, nsp7/8 or SARS-CoV-2 co-purified RTC and SARS-CoV-2 RTC + 100 μM **12b**, in presence and absence of 0.01% Tween 20 detergent, were pre-incubated on ice for 30 min 15 μL of each sample were mixed with 5 μL of NativePAGE® Sample Buffer (4X) and loaded in a 10-wells 3- 12% NativePAGE™ Novex® Bis-Tris gel. Samples were separated in 1X NativePAGE™ Anode Buffer (outer electrophoretic chamber) and 1X NativePAGE™ Dark Blue Cathode Buffer (inner electrophoretic chamber) for 120 min at 150 V constant. The already-stained gel was destained in 20% ethanol and 10% acetic acid. The gel image was acquired using ChemiDoc Imager (BioRad).

2.21. Crosslinking assay

Copurified SARS-CoV-2 RTC was preincubated with and without 100 μM of **12b** and suramin for 30 min at RT in reaction mix (20 mM HEPES pH 8.0, 10 mM DTT, 1 mM $MgCl_2$, 25 mM NaCl, 0.01% Tween20). Crosslinking reactions were performed with the addition of different concentrations of glutaraldehyde (0.05%, 0.025% and 0.013%) for 30 min at RT. Reactions were stopped with the addition of 100 mM Tris-HCl pH 8.0 and samples were loaded in 4-12% gradient SDS-PAGE.

2.22. Binding affinity determination

Binding affinity was determined using Monolith X (NanoTemper Technologies), which can measure both Spectral Shift (SpS) and MST/TRIC (Microscale Thermophoresis/Temperature Related Intensity Change) signals at the same time. The binding reactions were detected according to the manufacturer's instructions, with minor modifications. For compound affinity determination, 100 nM of SARS-CoV-2 co-purified RTC was labelled with a 50 nM solution of the RED-tris-NTA 2nd Generation dye (NanoTemper Technologies) and incubated at room temperature for 30 min, after which the sample was centrifuged at 15,000 g for 10 min and 4°C and transferred to a clean tube. Serial dilutions of the tested compound were prepared in H_2O (or DMSO for control compound suramin) and dispensed to the reaction mix (20 mM HEPES pH 8.0, 25 mM NaCl, 1 mM $MgCl_2$, 10 mM DTT, with 0.05% Tween 20) keeping a final concentration of 5% DMSO. In the case of H_2O-diluted nucleotide analogue, 5% DMSO was added to the reaction mix to keep binding conditions comparable to the control compound suramin.

For protein-protein binding affinity determination, purified SARS-CoV-2 nsp12 was labelled using the Spectral Shift Optimized Protein Labelling Kit – Lysine-Reactive (NanoTemper Technologies), following the manufacturer's protocol. For binding affinity determination, 100 nM of labelled SARS-CoV-2 nsp12 was incubated with serial dilutions of nsp7 or nsp8 at room temperature for 30 min in reaction mix (20 mM HEPES pH 8.0, 25 mM NaCl, 1 mM $MgCl_2$, 10 mM DTT, with 0.05% Tween 20), in absence or presence of 100 μM of compound **12b**.

Dose-dependent binding curves and K_D values by either SpS or MST/TRIC technologies were generated by the Monolith Evaluation software.

2.23. Antiviral activity of prodrug compounds

As previously described (Stefanelli et al., 2023), Vero E6-GFP cells were seeded in a black 96-well plate (ThermoFisher) at a density of 10^4 cells/well in DMEM supplemented with 10% heat-inactivated FBS (Gibco), 1% penicillin/streptomycin (Euroclone) and 0.075% Na-bicarbonate and incubated at 37°C in 5% CO_2. The following day, the cells were treated with serially diluted compounds in culture medium in presence of 2 μM P-gp inhibitor CP-100356 and infected -or mock-infected for cytotoxicity determination of compounds-with SARS-CoV-2 at a MOI of 0.01. After 72 h at 37°C, culture medium was removed and fluorescence at 485/535 nm, for exc/em wavelength respectively, was read with plate reader Victor Nivo (PerkinElmer). Dose-response curves of cell viability were generated with GraphPad Prism 10.1 by fitting the $\log_{10}$ compound concentration against the normalized fluorescence of treated cell viability vs non-treated controls using a variable-slope, non-linear regression. Compound GC376 was used as internal positive control (Vuong et al., 2020). Experiments were repeated in triplicate.

2.24. Biological resources

Stably transfected Vero E6 expressing GFP were acquired by Janssen Pharmaceutical. SARS-CoV-2 strain BetaCov/Belgium/GHB-03021/2020 was kindly provided by KU Leuven. SARS-CoV-2 nsp12, nsp7 and nsp8 plasmids were kindly provided by Dr. Marcin Nowotny (International Institute of Molecular and Cell Biology – Warsaw, Poland).

2.25. Statistical analyses

The statistical significance of the difference in total fluorescence intensity of the samples in the fluorescence polarization assay was calculated by using the non-parametric Mann-Whitney test with GraphPad Prism 10.1 for N = 3 replicates.

2.26. Receptor and ligand preparation

The three-dimensional (3D) X-Ray structure of the SARS-CoV-2 polymerase (nsp12) in the presence of cofactors nsp7 and nsp8 (PDB ID 7CXM) (Kim et al., 2020) was retrieved from the Protein Data Bank (www.rcsb.org). The structure was pre-processed using the Protein Preparation Wizard tool in the Maestro suite (Schrödinger Release, 2024-1) to assign bond orders, add hydrogen atoms, adjust disulfide bonds, and assign protonation states to residues at pH 7.4. Water molecules beyond 5 Å from heteroatoms were removed, and the structure was subjected to restrained minimization using the OPLS4 force field. The tridimensional structure of **12b** was generated using the graphical user interface (GUI) of Maestro. The LigPrep tool was used to optimize the ligand, and the protonation state at pH 7.4 in water was calculated using the Epik module(Shelley et al., 2007). Finally, the ligand geometry was minimized using the OPLS4 force field through 2500 iteration steps of the Polak−Ribiere Conjugate Gradient (PRCG) algorithm (Grippo and Lucidi, 1997).

2.27. Docking calculations

Docking was carried out using Schrödinger's Induced Fit Docking (IFD) workflow. First, SiteMap (SiteMap, S., LLC, New York, NY, USA, 2024) was used to identify druggable cavities, and grid-box coordinates were set based on the predicted site points (an inner box of 10 Å and an

automatically determined outer box to facilitate ligand sampling). The IFD workflow accounts for receptor flexibility, including side-chain and backbone adjustments, as well as ligand conformational sampling. No constraints were applied, and ten poses were saved, with a 2.5 kcal/mol energy window for ligand conformational sampling. The binding free energy (ΔG) was estimated using Prime MM-GBSA v3.000, which computes contributions from receptor, ligand, and complex energies, while accounting for strain effects.

2.28. Molecular Dynamics simulations (MDs)

The chosen docking pose and the Apo form of the nsp12–nsp7/8 complex underwent MD simulations using Desmond-v77135 (Schrödinger Release, 2024-1). Each system was solvated in a cubic TIP3P water box with a 22 Å buffer, neutralized with Na^+ and Cl^- ions, and adding 0.025 M NaCl to mimic physiological condition, yielding systems with more than 565.000 atoms. Energy minimization and equilibration were performed following Desmond protocols. The production MD simulations were run for 300 ns under NPT conditions (300 K, 1 atm) with a Langevin thermostat and barostat ($\tau = 5$ ps). Post-simulation analysis used *in-house* Python scripts, MDAnalysis for trajectory processing, and NumPy, SciPy, and Matplotlib for statistical analysis and visualization. The Desmond Simulation Interaction Diagram (SID) tool has been applied to examine ligand-protein interactions and generate data from MD trajectories. The Principal Component Analysis (PCA) was performed with the Apo system as a reference, aligning trajectories on backbone atoms to exclude translational and rotational motions. PCA was conducted separately for chain C (full backbone) and chain D (residues 90–192), focusing on regions near the ligand-binding site. Backbone coordinates from the Apo trajectory served as reference for PCA, and the first two principal components (PC1 and PC2) were retained. The complex trajectory was aligned to the Apo structure and projected onto the same PCA space for direct comparison. The free energy surface (FES) plots based on PC1–PC2 projections were created using Gaussian KDE, which generated isoenergy contours to compare conformational sampling between the Apo and complex states. For all in silico steps, the OPLS4 force field was used.

2.29. Computational resources and software

All calculations were carried out on NVIDIA RTX A5500 GPUs using GPU-accelerated Desmond, running on a Linux-based workstation (Dell Precision 7960 Tower). Trajectories were visualized with the Visual Molecular Dynamics (VMD) tool (Humphrey et al., 1996). All figures were rendered by UCSF Chimera (Pettersen et al., 2004) and Maestro GUI (Schrödinger Release, 2024-1).

3. Results

3.1. Compound synthesis

In light of their activity as chain terminators against the RT of HIV-1 and HIV-2 (Jia et al., 2020a, 2023), a series of six nucleotide analogues modified by the addition of a monoalkyl group in the γ-phosphate were synthesized. Compounds **11a**,**b** are acyclic 5-fluorouridine (5-FU) phosphonate derivatives, **12a**,**b** are (*S*)-HPMPC triphosphate derivatives, while **13a**,**b** are (*R*)-PMPA triphosphate derivatives (Fig. 2) (Jia et al., 2024).

Fig. 2. *Chemical structure and synthesis approach to the γ-monoalkyl modified triphosphate analogues of the nucleoside phosphonates and their acyloxybenzyl-prodrugs.* Reaction conditions: a) i. NCS, CH_3CN, THF, rt or 40°C 1-2 h; ii. $(Bu)_4N^+(H_2PO_4)^-$, CH_3CN, rt or 40°C, 1 h; b) i. TFAA, Et_3N, CH_3CN, 0°C 10 min; ii. 1-methylimidazol, Et_3N, DMF, 0°C, 10 min; iii. nucleoside phosphonate, DMF, THF, rt, 3 h; c) CH_3CN/$(n\text{-}Bu)_4N^+OH^-/H_2O$, rt, 24 h, Dowex 50WX8 (NH_4^+ form) ion exchange; d) i. NCS, CH_3CN, THF, rt or 40°C 1-2 h; ii. $(Bu)_4N^+(H_2PO_4)^-$, CH_3CN, rt or 40°C, 1 h; e) i. TFAA, Et_3N, CH_3CN, DMF, THF, 0°C 10 min; ii. 1-methylimidazol, Et_3N, CH_3CN, 0°C, 10 min; iii. nucleoside phosphonate, CH_3CN, rt, 2-5 h, Dowex 50WX8 (NH_4 form) ion exchange.

Three of these compounds were functionalized in the γ-phosphate with a single alkyl chain of 11 atoms of carbon (hereafter referred as 11-C), while the remaining three with a chain of 18 atoms of carbon (hereafter referred as 18-C). (*R*)-PMPA **1** was used because we already obtained good antiviral activity against HIV and the reverse transcriptase (Jia et al., 2024), (*S*)-HPMPC **3** was used as another prominent anti-HIV and anti-herpes antiviral as well as a known antitumor agent, while (*S*)-HPMPFU was used to enlarge the series of compounds with potential antitumor activity.

3.2. Stability of the CME-compounds against chemical or enzymatic hydrolysis

Chemical stability was studied first in phosphate buffer saline (PBS, pH 7.3). All monoalkylated triphosphate analogues proved to be highly stable under these conditions, e.g. **13b**: $t_{1/2}$ >200 h). Also, in CEM/0 cell extracts these compounds were not degraded, e.g. **13b**: $t_{1/2}$ >8 h (study was terminated after 8 h because of degradation of the cell extracts after this time) (Jia et al., 2024).

The corresponding acyloxybenzyl-alkyl-prodrugs of (*R*)-PMPA showed half-lives between 24 and 111 h in PBS yielding the γ-alkylated triphosphate analogues of the nucleoside phosphonates (Jia et al., 2024). The two AB-prodrugs of (*S*)-HPMPC and (*S*)-HPMPFU hydrolyzed with half-lives in PBS of 34 h (**15a**) and 21 h (**15b**) and 42 h (**16a**) and 28h (**16b**). As expected, the half-lives decreased in cell extracts due to the enzymatic cleavage of the prodrug moiety. Thus, the (*S*)-HPMPC derivative **15a** hydrolyzed with a half-life of 1.5 h while the (*S*)-HPMPUF derivative **16a** was cleaved with a half-life of 10 h. The difference here may be caused by the two different cell extracts; while the (*S*)-HPMPC compound was incubated in T-lymphocyte CEM/0 extracts, the HPMPUF compound was incubated in SW-620 tumor cell extracts.

3.3. Primary screening of nucleotide analogues against SARS-CoV-2 RTC

We proceeded to test these nucleotide analogues against the RdRp activity of SARS-CoV-2 nsp12 co-purified with cofactors nsp7 and nsp8 in a primer-elongation assay resolved by PAGE. Given that the nucleotide analogues were synthesized with different nucleobases, associated to different Watson-Crick pairings, and they lacked sugar moieties, we started with the evaluation of the ability of the polymerase to recognize and incorporate the analogues into the nascent RNA strand in the template-primer (T/P) complex (Fig. 3A). The assay was set up to substitute the related natural nucleotide with the triphosphate analogue and include the previously incorporated other nucleotides (e.g. a CTP analogue was evaluated in presence of GTP, given that the T/P substrate incorporates a guanine as first and cytosine as second base). No incorporation of the analogues could be detected in the presence of 100 μM of compounds and, instead, we observed complete loss of enzymatic activity for 18-C compounds and reduction of enzymatic activity for 11-C derivatives (Fig. 3B).

Fig. 3. ***(A)*** *Sequence of the RNA Cy5-labelled primer and unlabeled template complex used in the assay. The primer is* 20-nt *long with a 5′-Cy5 fluorophore label, while the unlabeled template is* 28-nt *long.* ***(B)*** *Denaturing PAGE of the primer elongation assay exploited to evaluate the potential of SARS-CoV-*2 RTC *to recognize and incorporate the tested NAs into the nascent strand. Different combinations of nucleotides were added according to the predicted complementarity of the analogue.* ***(C)*** *Lineweaver-Burk plot of the reciprocal initial velocities ($1/V_0$) versus the reciprocal concentrations of RNA substrate.* ***(D)*** *Lineweaver-Burk plot of the reciprocal initial velocities ($1/V_0$) versus the reciprocal concentrations of GTP substrate. The convergence of the lines on the negative X axis indicates the mechanism of action of a noncompetitive inhibitor in both panels.*

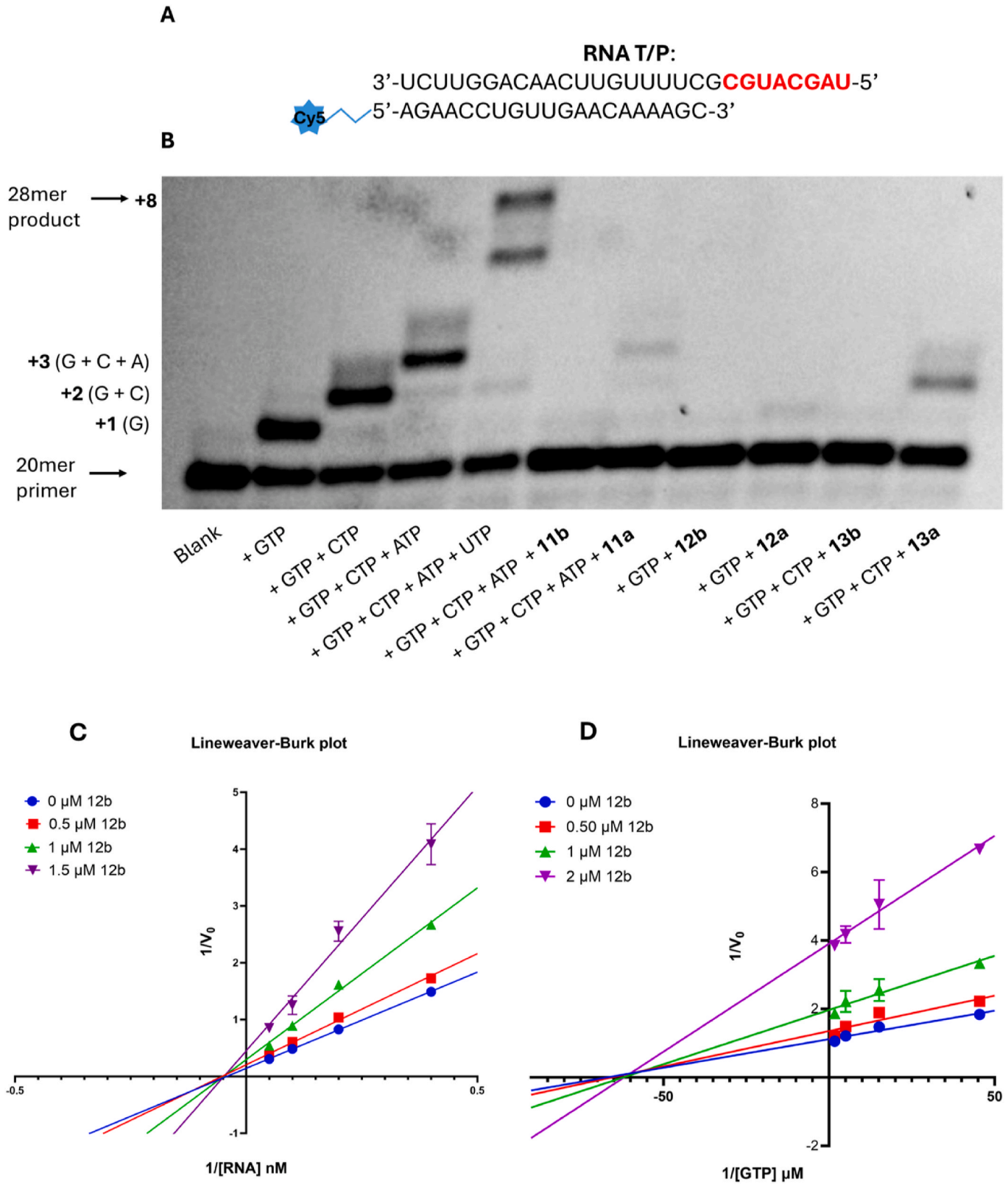

Fig. 3. Biochemical evaluation and mechanism of action of monoalkyl NAs.

In order to assess the inhibitory activity of the nucleotide analogues the presence of all four natural nucleotides, we evaluated the compounds at a single concentration of 100 μM in the presence of ATP, GTP, CTP and UTP, and we still obtained total inhibition of the polymerase activity for 18-C derivatives and a significant reduction (p value < 0.001, Mann-Whitney test) of activity for the 11-C derivatives (Supplementary Fig. S3).

3.4. Evaluation of dose-dependent activity of nucleotide analogues

To further assess the inhibitory activity of the γ-monoalkyl triphosphate analogues, we evaluated their dose-dependent inhibition of SARS-CoV-2 RTC starting from a concentration of 100 μM with 3-fold dilutions (Supplementary Fig. S4). Interestingly, we observed a similar IC_{50} value within the two groups of derivatives, either within the 18-C monoalkyl group or within the 11-C monoalkyl group (Supplementary Fig. S5). The IC_{50} values obtained for the 18-C derivatives were in the sub-micromolar range (Table 1).

To exclude nonspecific effects deriving from the alkyl chain alone, we also tested the C18-OH (1-octadecanol) and C18-monophosphate (octadecyl-1-phosphate) molecules against SARS-CoV-2 RdRp. Both molecules were found to be completely inactive at a concentration of 100 μM in the PAGE-based biochemical assay (data not shown).

3.5. Determination of the mechanism of action of alkyl-NAs

We then investigated the mechanism of action of the alkyl-NAs by assessing whether the compounds act as RNA or rNTPs competitors, therefore targeting the nsp12 active site. Given the higher potency of 18-C derivatives against the RdRp activity of SARS-CoV-2 in our enzymatic assay, we focused only on one 18-C derivative - namely CME1604 - for these characterizations.

We assessed the initial velocity of reaction using four different concentrations of substrates, either RNA or GTP, which represents the first nucleotide incorporated in the primer elongation assay (see Fig. 3A) and three different concentrations of compound, plus the condition of absence of compound that determines the control K_M and V_{max} parameters of the complex.

For each concentration of compound, by plotting the initial velocity versus the concentration of substrate (separately for either GTP or RNA), we fitted the results to the Michaelis-Menten equation. The calculated kinetics parameters obtained from the fit showed that the apparent K_M of both substrates did not change when increasing the concentration of compound, while the apparent V_{max} decreased in the competition assays both in the case versus RNA and versus GTP (Supplementary Fig. S6). This behavior is typical of a noncompetitive inhibitor.

These results were further confirmed by plotting the reciprocal initial velocity versus the reciprocal concentration of substrate - either RNA or GTP - in the Lineweaver-Burk plot. From linear regression of the data points, the convergence of the resulting lines on the negative half of the X-axis confirmed the noncompetitive behavior of the compound against both substrates of SARS-CoV-2 RdRp (Fig. 3C–D).

The same evaluation was performed for a pyrimidine, CTP, which is the natural counterpart of **12b** compound. Also in this case, the results showed a non-competitive mechanism of action (*data not shown*).

3.6. Evaluation of interference on RNA binding by alkyl-NAs

Considering how compound **12b** inhibits enzymatic activity without competing with either substrate of the RdRp, we proceeded to investigate whether **12b** could reduce RNA binding affinity of SARS-CoV-2 RTC due to the presence of its long terminal alkyl chain. To verify this, we exploited a fluorescence polarization (FP) assay, where binding of labelled RNA and SARS-CoV-2 RTC was determined by a 2-fold titration of enzyme concentration with a constant concentration of Cy5-labelled RNA T/P. The binding assay yielded a K_D value of 314.7 nM for the RNA substrate. The addition of a constant concentration of compound **12b** (6.6 μM, corresponding to 10-fold the IC_{50} value of the inhibitor) to the assay mix resulted in a K_D value of 1947 nM for the RNA, indicating that the tested compound is responsible for a ≈6-fold decrease in RNA binding affinity (Fig. 4A).

We also evaluated whether the variation in fluorescence might be due to an interference of compound autofluorescence, by calculating the total fluorescence intensity as the sum of RFU signal in the S plane and twice the value of the fluorescence in the P plane ($total\ RFU = RFU_S + 2 \times RFU_P$) (Markossian et al., 2004). The results of the nonparametric Mann-Whitney test show that the difference between the two conditions is not statistically significant (Fig. 4B), which confirms that no compound interference in the FP signal is present in the assay.

Fig. 4. ***(A)** Binding curve of SARS-CoV-2 RTC to the Cy5-labelled RNA substrate, in absence and presence of compound **12b**. The x axis shows the concentration of enzyme, while the y axis represents the delta of millipolarization (mP) signal. **(B)** The graph shows the total fluorescence intensity of the samples with and without compound. Mann-Whitney test revealed no statistically significant difference in RFU between the two conditions. **(C)** Native PAGE of the different isolated proteins of the RTC complex of SARS-CoV-2, the co-purified RTC complex and the RTC complex in presence of compound **12b**. The reactions were repeated in absence and presence of detergent Tween20®, at the same concentration used in the reaction mix of the enzymatic assay. The first lane shows the marker of different molecular weights. **(D)** SDS-PAGE of crosslinked SARS-CoV-2 with different concentrations of glutaraldehyde, in absence and presence of inhibitor **12b**. Suramin was used as negative control of dissociation.*

3.7. Assessing the effect of 12b on RNA binding

Given that the fluorescence polarization assay suggested a diminished affinity for RNA, while the competition assay revealed no competition between the RNA substrate and **12b**, we proceeded to investigate how the compound could interfere with the RNA binding by evaluating whether complex stability could be affected by the inhibitor. In fact, previous studies have shown that efficient RNA binding by nsp12 requires the presence of the cofactors nsp7 and nsp8 (Jones et al., 2022). To verify this hypothesis, we performed a native PAGE of the proteins forming the SARS-CoV-2 minimal RTC, in presence and absence of compounds (Fig. 4C).

Results showed that the presence of **12b** at a final concentration of 100 μM was able to induce RTC dissociation (Fig. 4C). Of note, the presence of two main bands at roughly the same height of nsp12 alone (lane 2) and associated nsp7/8 seems to suggest that the dissociation mostly involves nsp12 and the cofactors, while cofactors nsp7 and nsp8 appear to remain associated.

The same samples were also prepared in presence of 0.01% v/v Tween20 detergent, at the same concentration present in the reaction mix in which the inhibitory activity of the compounds was evaluated, given that the presence of the detergent itself could alter the oligomerization state of the complex. Results showed that the presence of the detergent did not change the **12b** inhibition pattern (Fig. 4C).

As confirmatory assay, we crosslinked the complex with glutaraldehyde in absence and presence of **12b**, to assess whether the compound - by dissociating the RTC - reduces the formation of covalent bonds between the complex components. Results showed that the presence of **12b** at 100 μM induces the dissociation of the complex at different concentrations of crosslinking agent glutaraldehyde, as compared to the DMSO controls. Suramin was used as negative control since it does not induce any dissociation of the complex, as observed in the resolved complex-ligand cryoEM structure (Yin et al., 2021) (Fig. 4D).

Table 1
IC_{50} values of γ-monoalkyl triphosphate nucleoside analogues.

SARS-CoV-2 RdRp IC_{50} (μM) [a]	
11-C derivative	**18-C derivative**
19.46 ± 0.44 (**11a**)	0.57 ± 0.18 (**11b**)
7.78 ± 1.8 (**12a**)	0.66 ± 0.11 (**12b**)
24.13 ± 4.25 (**13a**)	0.60 ± 0.09 (**13b**)

[a] IC_{50}: compound concentration required to inhibit by 50% the enzymatic activity.

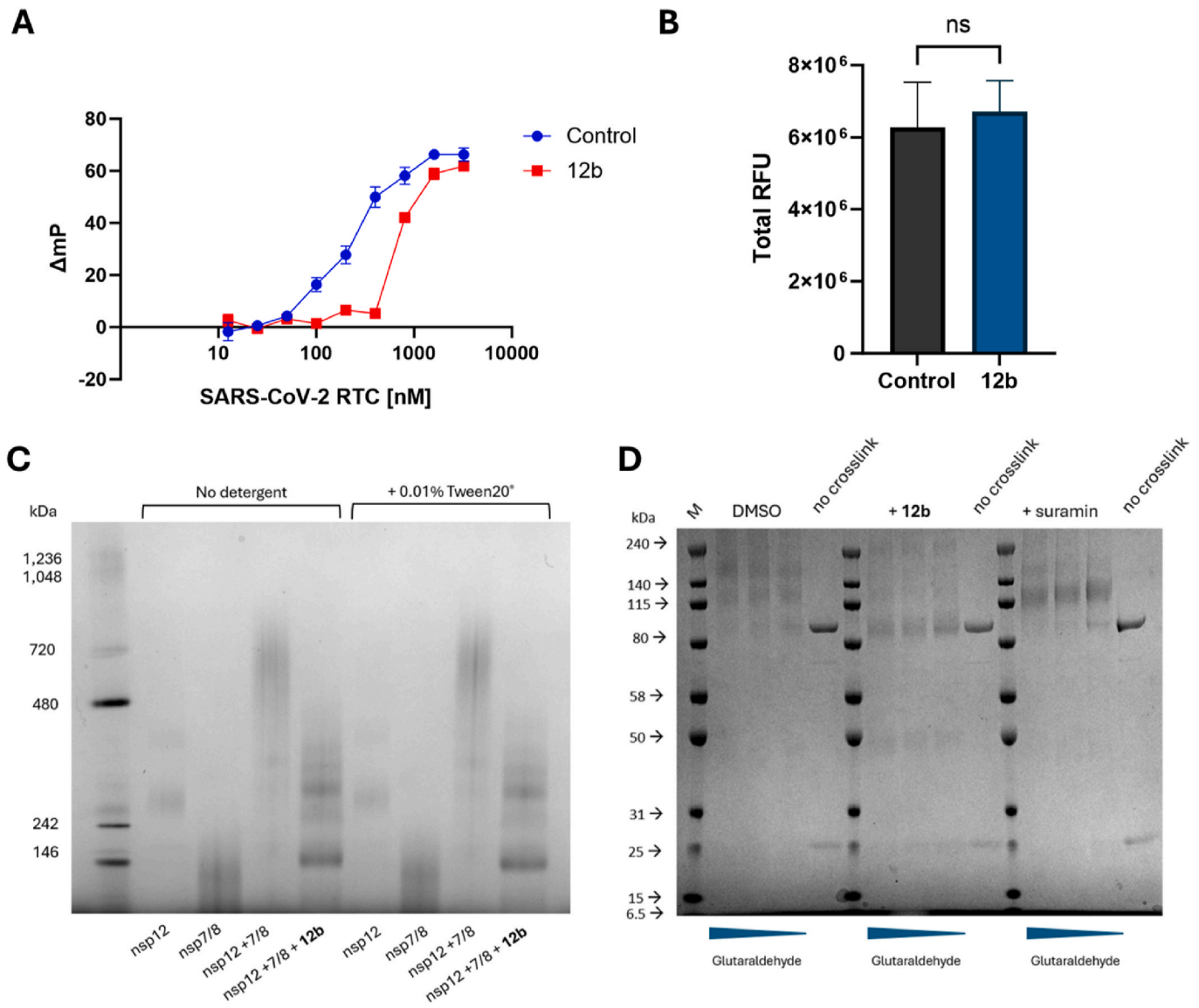

Fig. 4. γ-Monoalkyl triphosphate nucleoside analogues interference on RNA binding and complex stability.

3.8. Determination of binding affinity

To assess the binding affinity of compound **12b** to the SARS-CoV-2 RTC we used Microscale Thermophoresis/Temperature Related Intensity Change and Spectral Shift (MST/TRIC and SpS) technologies. Suramin was used as positive control, yielding a K_D of 606 ± 17 nM, in line with reported values (Schimunek et al., 2024; Yin et al., 2021) (Supplementary Fig. S7). In the case of compound **12b**, a K_D value of 38.7 ± 6.79 μM was obtained from the fit, confirming its specific binding to SARS-CoV-2 RTC (Supplementary Fig. S8A). We then asked whether we could measure **12b** binding affinity to the different protein forming the RTC. By performing binding assays with **12b** to isolated nsp12 or to co-purified nsp7/8 complex, we obtained K_D values of 138 and 58 μM for nsp12 and nsp7/8, respectively (data not shown). The fact that the IC_{50} value is in the submicromolar range, that the K_D values for both nsp12 and nsp7/8 are in the higher micromolar range, while the K_D value for the RTC complex is in a micromolar range in between the previous values, suggest that **12b** binding can dissociate the RTC through an interaction at a surface between nsp12 and nsp7 and/or nsp8.

To further investigate these possibilities and confirm the dissociation of the complex induced by the monoalkyl nucleotide analogues, we performed MST/SpS and assessed the effect of **12b** on the binding affinity of the two cofactors nsp7 and nsp8 to nsp12 (Supplementary Fig. S8B–C).

The interaction of nsp12 with nsp7 and nsp8 resulted in K_D values of 2.42 ± 1.39 and 5.12 ± 2.27 μM, respectively. When **12b** was added to the samples at the fixed concentration of 100 μM, nsp12 binding to nsp7 yielded a K_D value of 19.35 ± 3.89 μM, with a ≈8-fold increase as compared to the K_D value in absence of inhibitor (Supplementary Fig. S8D). In contrast, the interaction of nsp12 with nsp8 in the presence of 100 μM **12b** resulted in a K_D value of 5.04 ± 0.11 μM, with no appreciable variation as compared to the K_D value in absence of inhibitor (Supplementary Fig. S8E). Overall, these results demonstrate that **12b** dissociates the RTC by interacting with nsp12 and nsp7.

To further confirm the mechanism of action, we evaluated the inhibitory activity of compound **12b** on the RdRp activity monomeric NS5 of West Nile virus (WNV). We observed that the compound was not incorporated by the WNV NS5 into the nascent RNA strand (data not shown), and was neither able to inhibit its enzymatic function (Supplementary Fig. S9), in line with the proposed mechanism of inhibition targeting the assembly state of the oligomeric minimal RTC of SARS-CoV-2.

3.9. Allosteric druggable pocket identification and docking

To investigate the potential interaction of **12b** at the interface between nsp12 and nsp7, we first predicted druggable cavities in the nsp12–nsp8–nsp7 complex (PDB code: 7CXM) (Kim et al., 2020) using the SiteMap tool (SiteMap, S., LLC, New York, NY, USA, 2024). This approach identifies surface pockets and characterizes their molecular interaction fields, including hydrophobic regions (yellow), hydrogen-bond donors (blue), and hydrogen-bond acceptors (red). The analysis revealed a cavity of particular interest (SiteScore 1.016), located between the nsp12 catalytic domain and the nsp7 interface (Supplementary Fig. S10), suggesting a structurally permissive area potentially compatible with small-molecule binding. Therefore, to predict the putative binding mode of **12b**, Induced Fit Docking (IFD) followed by MM-GBSA calculations was conducted (Glide and Prime, S., LLC, New York, NY, USA, 2024). Taking into account the theoretical affinity values, the best-ranked pose (GScore: −7.183 kcal/mol; IFD score: −67597.68 kcal/mol; MM-GBSA ΔG: −28.18 kcal/mol) was selected as a representative binding hypothesis and subjected to a 300 ns conventional Molecular Dynamics (MD) simulation to evaluate its dynamic stability and to explore potential conformational changes, using the Apo form as a control. Notably, other top-ranked poses exhibited binding geometries that were highly similar, supporting the robustness and consistency of the predicted interaction mode.

3.10. MD simulations

The analysis of the MD trajectory of nsp12-nsp7-nsp8 in complex with **12b** supports the stability of the predicted docking pose. The long alkyl chain of the γ-phosphonate occupies the interfacial cavity between nsp12-nsp8 and nsp7, while the nucleoside core maintains persistent contacts with residues K97 and V160 of nsp8^{I}, as well as T402, N403, and F407 of nsp12. Additional hydrophobic contacts, especially with F407 of nsp12, further stabilize this interaction pattern (Fig. 5A–B). Consistently, the *ligand Root Mean Square Deviation* (L-RMSD) plot shows stabilization after an initial adjustment phase, supporting the presence of dynamically stable interactions throughout the simulation (Fig. 5C).

Fig. 5. *Overview of the nsp12–nsp7–nsp8 complex in the presence of* ***12b****.* ***(A)*** *A three-dimensional (3D) cartoon representation of the complex, with structural regions distinctly colored and labelled. The zoomed view illustrates the putative binding mode of* ***12b****, shown in a stick representation, with key interacting residues displayed and labelled as sticks.* ***(B)*** *Interaction fraction plot depicting residue-ligand interactions over the* 300 ns *of MDs.* ***(C)*** *Ligand RMSD plot (L-RMSD) profile of* ***12b*** *throughout the* 300 ns *MDs.* ***(D-E)*** *Principal component analysis (PCA) of nsp7 (chain C) and nsp8^{II} (chain D, residues 90–192) of the two systems (Apo vs.* ***12b****–bound system).* ***D)*** *MD trajectories are projected onto the first two principal components (PC1 and PC2), using the apo structure as a reference, for chain C (left) and chain D (right).* ***E)*** *Free energy contour maps depict the conformational space sampled in Apo and* ***12b****–bound states. The presence of* ***12b*** *induces a measurable reorganization of the accessible conformational landscape, with distinct effects observed for the two chains.*

3.11. Free energy surface and principal component analyses

Subsequently, free energy surface (FES) and principal component (PC) analyses were performed on the MD trajectories to identify energetic minima and enable a quantitative comparison of the sampled conformational landscape between the two systems (Apo *vs.* **12b**-Complex). The analysis mainly focused on the nsp7 (*C-chain*) and the adjacent nsp8^{II} interface region (residues 90–192 of the *D-chain),* which are directly involved in the interfacial dynamics of the complex (Fig. 5D–E and Supplementary Fig. S10). In the Apo system, the free energy landscape is characterized by a dominant and deep minimum, accompanied by two conformational transition pathways (Supplementary Fig. S11A). In contrast, the **12b**–bound complex exhibits a reorganized free-energy profile characterized by two minima, one of which is significantly deeper and more localized (Supplementary Fig. S11B), suggesting a ligand-induced stabilization of a specific interfacial conformation. To relate these energetic features to structural rearrangements, representative conformations corresponding to the main free energy minima were extracted and structurally analyzed, enabling correlation between the observed energetic features and ligand-associated conformational rearrangements within the interface region (Supplementary Fig. S11C–D).

PCA projections showed differences in both the variance along PC1 and PC2 and the size of the conformational space sampled between chain C (nsp7) and chain D (nsp8^{II}) in the Apo and **12b**–bound states (Fig. 5D). In the complex, Chain C shows a reduction in PCA variance and conformational space, indicating a slight structural change. This effect is consistent with the substantial overlap of nsp7 alpha helices between Apo and bound states. In contrast, chain D (nsp8^{II}) in the complex exhibits more pronounced conformational deviations from the Apo form. The isoenergetic plots of the C and D chains further clarify differences between the two systems, with the changes more evident for the D chain (Fig. 5E).

In this view, it is important to note that although the C chain is structurally constrained between neighboring regions and stabilized by strong electrostatic interactions, a subtle yet detectable shift is present. This is reflected in the displacement of its three alpha-helices in both the Apo and Complex systems (Fig. 6).

Fig. 6. *3D structural alignment of Apo and Complex structures. Top panels: Cartoon representations of the aligned structures viewed from the front (left) and back (right) perspectives. In the center panel, a surface representation illustrates the aligned Apo and Complex structures, emphasizing key structural differences. Nsp12, nsp8 (chains B/D), nsp7 (chain C), and RNA are color-coded as specified.* ***12b*** *is depicted in CPK style. Arrows indicate ligand-driven conformational changes shifts in nsp7 and nsp8, suggesting an allosteric influence propagated through the polymerase complex.*

This confirms that the ligand exerts a measurable structural influence even in the most rigid parts of the complex. Collectively, the data support a model in which **12b** occupies an interfacial position between nsp12 and nsp7, with the highly flexible alkyl chain perturbing local interfacial organization, leading to progressive disordering of the nsp12–nsp7–nsp8 interface rather than inducing large-scale structural rearrangements. While the timescale of the MD simulations does not capture a complete subunit dissociation event, the observed structural and dynamical perturbations are consistent with an early-stage disordering process. In this context, and in light of the available experimental evidence, these computational results support the hypothesis that progressive interface destabilization may ultimately facilitate nsp7 dissociation from the complex, providing a mechanistic framework linking the observed molecular interactions to the experimentally detected functional effects. This model may explain the observed difference in the activity of the C18 and C11 derivatives. A C18 alkyl chain provides substantially greater hydrophobic surface area and can form significantly more van der Waals contacts within the nsp12–nsp7 interfacial groove than a C11 chain. Those additional contacts increase binding affinity and residence time, enabling the alkyl tail to wedge between side chains and subtly displace helices, which produces the progressive local disordering observed in simulations.

3.12. In vitro antiviral activity of prodrugs against SARS-CoV-2

To evaluate the biological activity of the compounds on viral replication in cell culture, different prodrugs of the γ-phosphate monoalkyl NAs were synthesized. The prodrugs are linked to bioreversible mask groups made of acyloxybenzyl moieties in the γ-phosphate, to minimize the effects of the negative charges of the triphosphate group on cell membrane permeability. Prodrugs **14a-d** derive from **13b** compound; prodrugs **15a**,**b** derive from **12a**,**b** compounds, while **16a**,**b** are derivatives of compound **11b**. All prodrugs deriving from the same

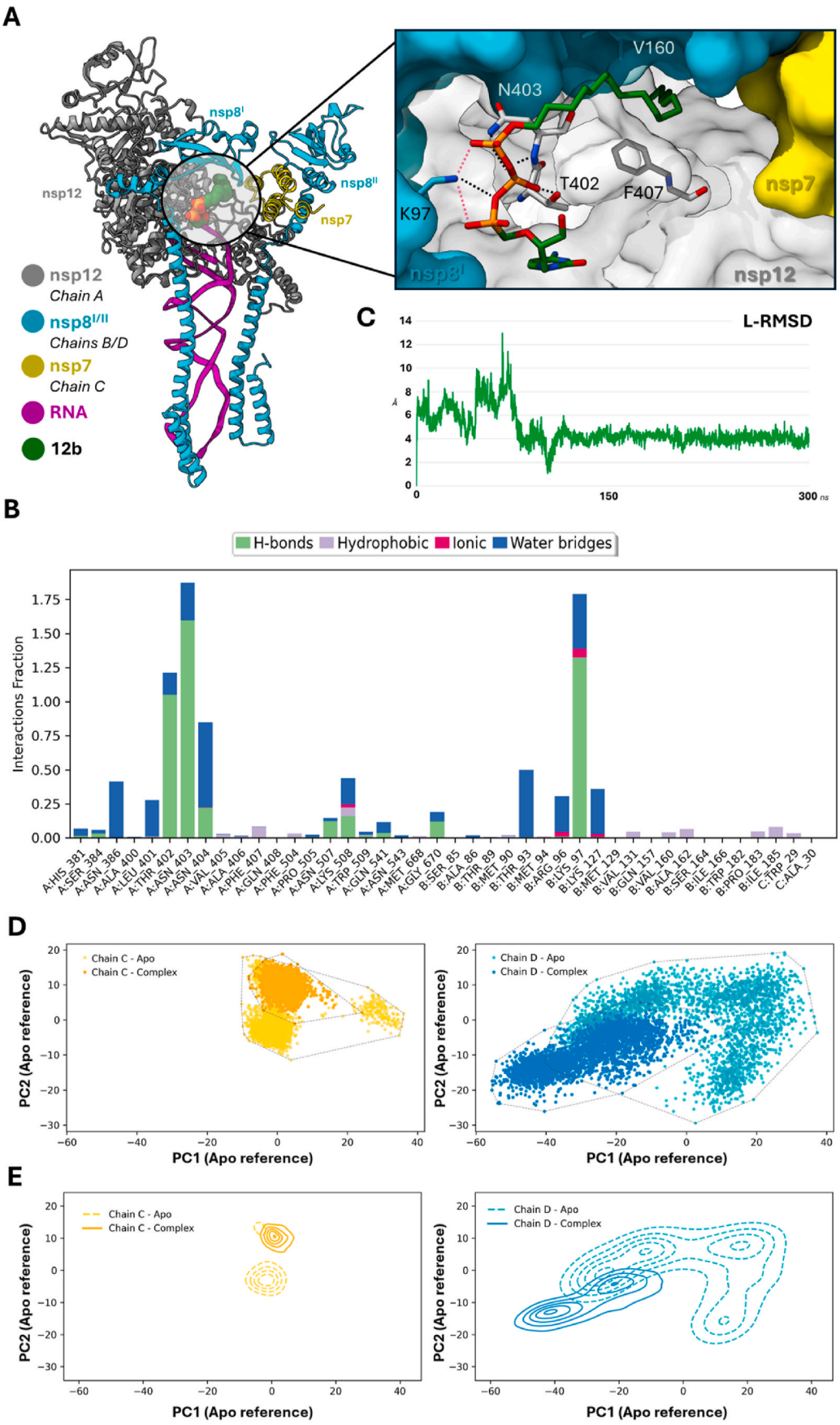

Fig. 5. Molecular dynamics and conformational analysis of the SARS-CoV-2 RTC in complex with compound 12b.

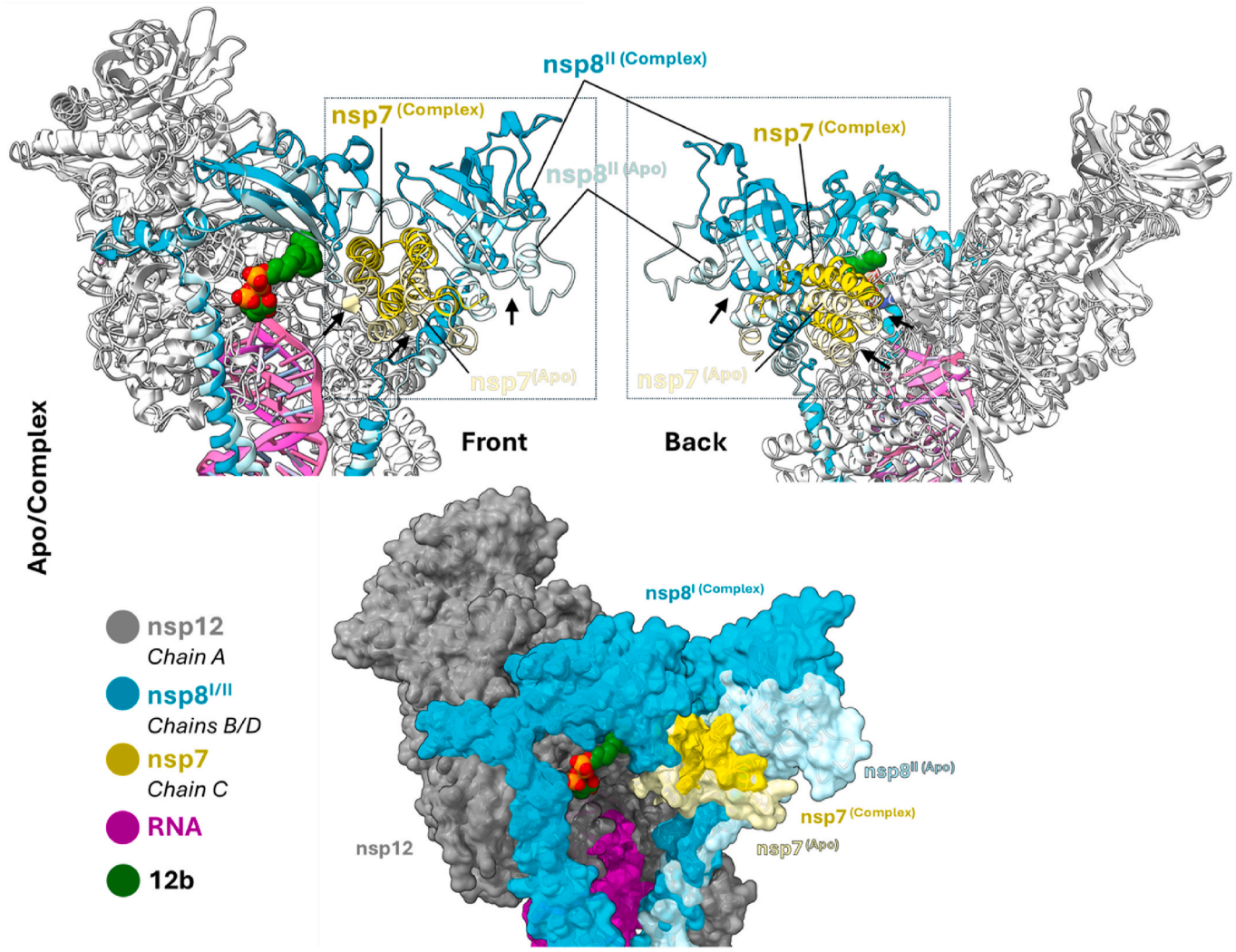

Fig. 6. 3D structural alignment of Apo and Complex structures

compound differ one from another only by the length of the alkoxy group (Fig. 1).

Treatment of infected or mock infected cells with 3-fold serially diluted compounds allowed to determine the cytotoxicity and the antiviral activity of the prodrugs. SARS-CoV-2 3CLpro covalent inhibitor GC376 was used as positive control (Fu et al., 2020; Luan et al., 2023) (Table 2). Results showed that some of the compounds possess a moderate inhibitory activity against the replication of SARS-CoV-2 *in vitro*, displaying EC_{50} values between 24 and 79 μM, while others resulted inactive. In general, the compounds displayed low cytotoxicity, with CC_{50} values above 60 μM, with selectivity indexes between 2 and 3 for the active compounds.

4. Discussion

In the present work, we evaluated the ability of a series of mono-alkylated triphosphate acyclic nucleotide analogues to inhibit the RdRp activity of SARS-CoV-2 in a biochemical assay, and the derivative prodrugs on SARS-CoV-2 replication *in vitro*.

These analogues derive from known scaffolds, namely 5-fluorouracil (5-FU), HPMPC and PMPA. HPMPC is an acyclic nucleotide analogue approved for the treatment of CMV-induced retinitis by acting as the prodrug of cidofovir diphosphate, and it is active against a panel of other DNA viruses (De Clercq and Li, 2016). HPMPC diphosphate was proved to be incorporated by SARS-CoV-2 RdRp, acting as a delayed chain terminator (Jockusch et al., 2020), similar to remdesivir triphosphate, which induces a steric hindrance at the position of three nucleotides

Table 2
Dose-dependent activity determination against SARS-CoV-2 replication in Vero E6 GFP cells.

Compound	SARS-CoV-2 EC_{50} ± SD [a] (μM)	Vero E6 GFP CC_{50} ± SD [b] (μM)	Selectivity index [c]
14a	>98	98.01 ± 1.63	-
14b	24.94 ± 9.62	72.26 ± 18.19	2.90
14c	50.4 ± 13.85	97.54 ± 3.49	1.94
14d	>100	>100	-
15a	79.32 ± 12.25	>100	>1.26
15b	>100	>100	-
16a	>61	61.16 ± 34.73	-
16b	>100	>100	-
GC376	0.44 ± 0.001	>100	>226

The table shows the EC_{50}, CC_{50} and SI values for each compound. GC76 was used as positive control.

[a] EC_{50} represents the compound concentration required to inhibit viral replication by 50%.

[b] CC_{50} represents the compound concentration required to kill 50% of the cells, compared to untreated controls.

[c] The selectivity index represents the therapeutic window, calculated as the ratio of the CC_{50} and EC_{50}.

post-incorporation (Gordon et al., 2020). PMPA is an acyclic nucleoside phosphonate analogue, approved by the FDA for the treatment of HBV and HIV; it competes with dATP, inducing immediate chain termination of the viral polymerases (De Clercq and Li, 2016). PMPA has been evaluated against SARS-CoV-2, and it was demonstrated that it is recognized and incorporated by nsp12 into the nascent RNA strand, inducing immediate chain termination (Chien et al., 2020; Jockusch et al., 2020; Wang et al., 2022). Moreover, a phase II clinical trial on a cohort of sixty patients demonstrated that a combination of tenofovir and emtricitabine accelerates the clearance of nasopharyngeal SARS-CoV-2 viral load (Parienti et al., 2021). 5-FU is a widely known and used drug for the treatment of solid malignant tumors, where it induces cytotoxic effects via incorporation into the cellular DNA and the induction of a toxic mutational burden (Christensen et al., 2019; Longley et al., 2003). 5-FU has been shown to be incorporated by the coronaviruses RdRp of Murine Hepatitis Virus (MHV), (Middle East Respiratory Syndrome) MERS-CoV and SARS-CoV, increasing mutational frequency, although its effects are mitigated by its removal from the viral genome by the proofreading activity of the ExoN complex (Ogando et al., 2020; Smith et al., 2013), as observed for other incorporated analogues such as remdesivir monophosphate (Yang et al., 2025).

We synthesized a series of HPMPC, PMPA and 5-FU derivatives, each characterized by the presence of a single alkyl chain linked to the γ-phosphate group, with either 11 (11-C) or 18 (18-C) atoms of carbon. Since similar compounds were shown to be active against the HIV-1 and HIV-2 RTs, which incorporated the analogues into the nascent strand inducing a premature polymerase arrest (Jia et al., 2020b, 2023; Zhao et al., 2020), we tested whether also the RdRp of SARS-CoV-2 could similarly incorporate these analogues. Substitutions were made based on predicted complementarity in the sequence of incorporation. Unexpectedly, we observed not only a lack of analogue incorporation into the elongated primer, but also a substantial to complete reduction in overall enzymatic activity.

The alkyl chain length emerged as the primary determinant of potency, with 18-C derivatives showing 10-40-fold greater activity than 11-C analogues, while nucleobases had minimal impact. This structure-activity relationship indicates that lipophilic alkyl chain drives the inhibition of the RdRp activity rather than base-pairing specificity at the catalytic site. The noncompetitive inhibition kinetics further support this mechanism, as K_M values for both RNA and nucleotide substrates remained constant while V_{max} decreased, consistent with an allosteric mode of action impairing catalytic turnover without blocking substrate processing. Binding affinity measurements further strengthen this pattern that suggests a mechanism of protein-protein disruption. In fact, the K_D of **12b** for the intact RTC (38.7 μM) is substantially lower than for isolated nsp12 (138 μM) or nsp7/8 (58 μM), suggesting preferential recognition of the assembled complex. The discrepancy between the K_D and the IC_{50} value obtained for **12b** may reflect transient interactions with RTC components, rapidly dissociating upon inhibitor binding to the fully assembled RTC in the enzymatic assay.

The dramatic 8-fold increase in nsp12-nsp7 K_D upon addition of **12b**, in contrast with the unchanged nsp12-nsp8 affinity, indicates nsp7 dissociation as the key event in RTC inactivation, further supported by native-PAGE and crosslinking assay. This selectivity is particularly significant, as nsp7 plays a critical role in stabilizing nsp12 and maintaining the RNA binding channel geometry (Singh et al., 2025). The 6-fold reduction in RNA binding affinity observed in fluorescence polarization assays can therefore be explained as a direct consequence of nsp7 loss, which destabilizes the RNA-binding competent conformation of nsp12 (Jones et al., 2022).

The Site Map and docking simulations data supports a model in which **12b** occupies an interfacial position between nsp12 and nsp7. Subsequent MD simulations further confirmed the proposed mechanism and demonstrated the stability of ligand interactions over time. The γ-phosphate alkyl chain perturbs local interfacial organization, with subtle effects on the structurally constrained nsp7 and more pronounced changes at the flexible $nsp8^{II}$ region, consistent with early-stage interface destabilization rather than large-scale structural rearrangements. FES and PCA analyses provide a mechanistic rationale linking molecular interactions to the experimentally observed functional effects. The structural perturbations observed in the MD simulations are consistent with a potential pathway for nsp7 dissociation from the replication complex. Furthermore, the predicted binding mode offers a framework for rational optimization of **12b**, guiding the development of more potent replication inhibitors. In fact, since the RTC perturbation has been shown to be primarily driven by the flexible alkyl tail, its effect is largely independent of the ligand's base, therefore modifying the terminal cap might offer a tractable route to tune potency and selectivity. Optimal chain length should also be investigated: intermediate and longer lengths may reveal an optimum where hydrophobic burial, steric accommodation, and entropic cost are balanced to maximize interface destabilization without incurring steric clashes or excessive desolvation penalties.

Additionally, we determined whether this series of monoalkylated nucleotide analogues could inhibit SARS-CoV-2 replication *in vitro*. A series of prodrugs of the γ-monoalkyl triphosphate analogues were synthesized, with a single biodegradable acyloxybenzyl mask group to reduce phosphate backbone charges and facilitate cell entry. The masking group is removed intracellularly by esterases, releasing the γ-alkylated nucleoside triphosphate form and bypassing the classical phosphorylation steps (Jia et al., 2020a). The biological evaluation of prodrugs revealed moderate antiviral activity (EC_{50} 25-79 μM) with acceptable selectivity indices. The C_4-alkyl masking group provided optimal balance between stability and cellular permeability, as evidenced by the antiviral activity of **14b**. However, the gap between biochemical potency and cellular efficacy indicates delivery challenges that must be addressed through further prodrug optimization.

5. Conclusions

In conclusion, this study identifies, to the best of our knowledge, a novel mechanism of action against SARS-CoV-2 RdRp, providing the basis for the development of antiviral compounds. Enhancing potency against viral replication inhibition will require more stable and selective derivatives, potentially offering novel tools for combating SARS-CoV-2 infections. Moreover, these findings open avenues for the rational design and development of novel inhibitors targeting the protein-protein interactions, highlighting a promising strategy for future antiviral therapeutics.

CRediT authorship contribution statement

Paolo Malune: Conceptualization, Data curation, Investigation, Visualization, Writing – original draft. **Giuliano Kullik:** Investigation, Validation, Writing – review & editing. **Xiao Jia:** Investigation, Validation, Writing – review & editing. **Gyde Bandowski:** Investigation, Validation, Writing – review & editing. **Francesca Esposito:** Supervision, Writing – review & editing. **Antonio Lupia:** Formal analysis, Investigation, Visualization, Writing – original draft. **Simona Distinto:** Formal analysis, Investigation, Visualization, Writing – original draft. **Elias Maccioni:** Conceptualization, Funding acquisition, Project administration, Supervision, Writing – review & editing. **Chris Meier:** Conceptualization, Funding acquisition, Project administration, Supervision, Writing – review & editing. **Enzo Tramontano:** Conceptualization, Funding acquisition, Project administration, Supervision, Writing – review & editing.

Declaration of competing interests

The authors declare that they have no known competing financial interests or personal relationships that could have appeared to influence the work reported in this paper.

Acknowledgments

This research was supported by EU funding within the NextGeneration EU-MUR PNRR - M4C2 I1.3. Extended Partnership initiative on Emerging Infectious Diseases (Project no.PE00000007, INF-ACT) spoke 5 and by RAS LR 7/07 project VIR-UNICA F73C22001570002. CM thanks Hamburg University and the Deutsche Forschungsgemeinschaft (DFG, German Research Foundation) –SFB 1648/1 2024 –512741711 for financial support. Graphical Abstract was created in BioRender.

Appendix A. Supplementary data

Supplementary data to this article can be found online at https://doi.org/10.1016/j.antiviral.2026.106514.

Data availability

No data was used for the research described in the article.

References

Balzarini, J., Holy, A., Jindrich, J., Naesens, L., Snoeck, R., Schols, D., De Clercq, E., 1993. Differential antiherpesvirus and antiretrovirus effects of the (S) and (R) enantiomers of acyclic nucleoside phosphonates: potent and selective in vitro and in vivo antiretrovirus activities of (R)-9-(2-phosphonomethoxypropyl)-2,6-diaminopurine. Antimicrob. Agents Chemother. 37, 332–338. https://doi.org/10.1128/AAC.37.2.332.

Brodfuehrer, P.R., Howell, H.G., Sapino, C., Vemishetti, P., 1994. A practical synthesis of (S)-HPMPC. Tetrahedron Lett. 35, 3243–3246. https://doi.org/10.1016/S0040-4039(00)76875-4.

Chien, M., Anderson, T.K., Jockusch, S., Tao, C., Li, X., Kumar, S., Russo, J.J., Kirchdoerfer, R.N., Ju, J., 2020. Nucleotide analogues as inhibitors of SARS-CoV-2 polymerase, a key drug target for COVID-19. J. Proteome Res. 19, 4690–4697. https://doi.org/10.1021/acs.jproteome.0c00392.

Christensen, S., Van der Roest, B., Besselink, N., Janssen, R., Boymans, S., Martens, J.W. M., Yaspo, M.-L., Priestley, P., Kuijk, E., Cuppen, E., Van Hoeck, A., 2019. 5-Fluorouracil treatment induces characteristic T>G mutations in human cancer. Nat. Commun. 10, 4571. https://doi.org/10.1038/s41467-019-12594-8.

Clercq, E. De, Andrei, G., Balzarini, J., Hatse, S., Liekens, S., Naesens, L., Neyts, J., Snoeck, R., 1999. Antitumor potential of acyclic nucleoside phosphonates. Nucleosides Nucleotides 18, 759–771. https://doi.org/10.1080/15257779908041563.

Clercq, E. De, Holý, A., 2005. Acyclic nucleoside phosphonates: a key class of antiviral drugs. Nat. Rev. Drug Discov. 4, 928–940. https://doi.org/10.1038/nrd1877.

Clercq, E. De, Sakuma, T., Baba, M., Pauwels, R., Balzarini, J., Rosenberg, I., Holý, A., 1987. Antiviral activity of phosphonylmethoxyalkyl derivatives of purine and pyrimidines. Antivir. Res. 8, 261–272. https://doi.org/10.1016/S0166-3542(87)80004-9.

De Clercq, E., 2004. Antiviral drugs in current clinical use. J. Clin. Virol. 30, 115–133. https://doi.org/10.1016/j.jcv.2004.02.009.

De Clercq, E., Li, G., 2016. Approved antiviral drugs over the past 50 years. Clin. Microbiol. Rev. 29, 695–747. https://doi.org/10.1128/CMR.00102-15.

European Medicines Agency, 2023. Lagevrio (molnupiravir) [WWW Document]. https://www.ema.europa.eu/en/medicines/human/EPAR/lagevrio. URL (accessed 11.1.24).

Fu, L., Ye, F., Feng, Y., Yu, F., Wang, Q., Wu, Y., Zhao, C., Sun, H., Huang, B., Niu, P., Song, H., Shi, Y., Li, X., Tan, W., Qi, J., Gao, G.F., 2020. Both Boceprevir and GC376 efficaciously inhibit SARS-CoV-2 by targeting its main protease. Nat. Commun. 11, 4417. https://doi.org/10.1038/s41467-020-18233-x.

Gordon, C.J., Tchesnokov, E.P., Woolner, E., Perry, J.K., Feng, J.Y., Porter, D.P., Götte, M., 2020. Remdesivir is a direct-acting antiviral that inhibits RNA-dependent RNA polymerase from severe acute respiratory syndrome coronavirus 2 with high potency. J. Biol. Chem. 295, 6785–6797. https://doi.org/10.1074/jbc.RA120.013679.

Grippo, L., Lucidi, S., 1997. A globally convergent version of the Polak-Ribière conjugate gradient method. Math. Program. 78, 375–391. https://doi.org/10.1007/BF02614362.

Humphrey, W., Dalke, A., Schulten, K., 1996. VMD: visual molecular dynamics. J. Mol. Graph. 14, 33–38. https://doi.org/10.1016/0263-7855(96)00018-5.

Jia, X., Kullik, G.A., Bufano, M., Brancale, A., Schols, D., Meier, C., 2024. Membrane-permeable tenofovir-di- and monophosphate analogues. Eur. J. Med. Chem. 264, 116020. https://doi.org/10.1016/j.ejmech.2023.116020.

Jia, X., Schols, D., Meier, C., 2020a. Lipophilic triphosphate prodrugs of various nucleoside analogues. J. Med. Chem. 63, 6991–7007. https://doi.org/10.1021/acs.jmedchem.0c00358.

Jia, X., Schols, D., Meier, C., 2023. Pronucleotides of 2′,3′-Dideoxy-2′,3′-Didehydrothymidine as potent Anti-HIV compounds. J. Med. Chem. 66, 12163–12184. https://doi.org/10.1021/acs.jmedchem.3c00755.

Jia, X., Weber, S., Schols, D., Meier, C., 2020b. Membrane permeable, bioreversibly modified prodrugs of nucleoside Diphosphate-γ-Phosphonates. J. Med. Chem. 63, 11990–12007. https://doi.org/10.1021/acs.jmedchem.0c01294.

Jockusch, S., Tao, C., Li, X., Anderson, T.K., Chien, M., Kumar, S., Russo, J.J., Kirchdoerfer, R.N., Ju, J., 2020. A library of nucleotide analogues terminate RNA synthesis catalyzed by polymerases of coronaviruses that cause SARS and COVID-19. Antivir. Res. 180, 104857. https://doi.org/10.1016/j.antiviral.2020.104857.

Johnson, K.A., Goody, R.S., 2011. The original Michaelis constant: translation of the 1913 Michaelis–Menten paper. Biochemistry 50, 8264–8269. https://doi.org/10.1021/bi201284u.

Jones, A.N., Mourão, A., Czarna, A., Matsuda, A., Fino, R., Pyrc, K., Sattler, M., Popowicz, G.M., 2022. Characterization of SARS-CoV-2 replication complex elongation and proofreading activity. Sci. Rep. 12, 9593. https://doi.org/10.1038/s41598-022-13380-1.

Kabinger, F., Stiller, C., Schmitzová, J., Dienemann, C., Kokic, G., Hillen, H.S., Höbartner, C., Cramer, P., 2021. Mechanism of molnupiravir-induced SARS-CoV-2 mutagenesis. Nat. Struct. Mol. Biol. 28, 740–746. https://doi.org/10.1038/s41594-021-00651-0.

Kim, D., Lee, J.-Y., Yang, J.-S., Kim, J.W., Kim, V.N., Chang, H., 2020. The architecture of SARS-CoV-2 transcriptome. Cell 181, 914–921.e10. https://doi.org/10.1016/j.cell.2020.04.011.

Kullik, G.A., 2023. Synthese Von Acyclischen Phosphonat-Diphosphat-Prodrugs. University of Hamburg. Ph.D. thesis.

Lineweaver, H., Burk, D., 1934. The determination of enzyme dissociation constants. J. Am. Chem. Soc. 56, 658–666. https://doi.org/10.1021/ja01318a036.

Longley, D.B., Harkin, D.P., Johnston, P.G., 2003. 5-Fluorouracil: mechanisms of action and clinical strategies. Nat. Rev. Cancer 3, 330–338. https://doi.org/10.1038/nrc1074.

Lu, G., Zhang, X., Zheng, W., Sun, J., Hua, L., Xu, L., Chu, X., Ding, S., Xiong, W., 2020. Development of a simple *in vitro* assay to identify and evaluate nucleotide analogs against SARS-CoV-2 RNA-dependent RNA polymerase. Antimicrob. Agents Chemother. 65. https://doi.org/10.1128/AAC.01508-20.

Luan, X., Chen, B., Shang, W., Yin, W., Jin, Y., Zhang, L., Xu, H.E., Zhang, S., 2023. Structure basis for inhibition of SARS-CoV-2 by the feline drug GC376. Acta Pharmacol. Sin. 44, 255–257. https://doi.org/10.1038/s41401-022-00929-z.

Madru, C., Tekpinar, A.D., Rosario, S., Czernecki, D., Brûlé, S., Sauguet, L., Delarue, M., 2021. Fast and efficient purification of SARS-CoV-2 RNA dependent RNA polymerase complex expressed in Escherichia coli. PLoS One 16, e0250610. https://doi.org/10.1371/journal.pone.0250610.

Malone, B., Urakova, N., Snijder, E.J., Campbell, E.A., 2022. Structures and functions of coronavirus replication–transcription complexes and their relevance for SARS-CoV-2 drug design. Nat. Rev. Mol. Cell Biol. 23, 21–39. https://doi.org/10.1038/s41580-021-00432-z.

Malune, P., 2025. Identification and characterization of the mechanisms of action of novel antiviral compounds targeting the minimal replication-transcription complex of SARS-CoV-2. Università Degli Studi Di Cagliari.

Markossian, S., Grossman, A., Arkin, M., Auld, D., Austin, C., Baell, J., Brimacombe, K., Chung, T.D.Y., Coussens, N.P., Dahlin, J.L., Devanarayan, V., Foley, T.L., Glicksman, M., Gorshkov, K., Haas, J.V., Hall, M.D., Hoare, S., Inglese, J., Iversen, P. W., Lal-Nag, M., Li, Z., Jason, Manro, R., Mcgee, J., Mcmanus, O., Pearson, M., Riss, T., Saradjian, P., Sitta, G., Mike, S., Trask, T.O.J., Weidner, J.R., Mary, Wildey, J., Wilson, K., Menghang Xia, Xu, X., 2004. Assay Guidance Manual Last Updated:, 31, 2.02.

Ogando, N.S., Zevenhoven-Dobbe, J.C., van der Meer, Y., Bredenbeek, P.J., Posthuma, C. C., Snijder, E.J., 2020. The enzymatic activity of the nsp14 exoribonuclease is critical for replication of MERS-CoV and SARS-CoV-2. J. Virol. 94. https://doi.org/10.1128/JVI.01246-20.

Okoli, G.N., Rabbani, R., Copstein, L., Al-Juboori, A., Askin, N., Abou-Setta, A.M., 2021. Remdesivir for coronavirus disease 2019 (COVID-19): a systematic review with meta-analysis and trial sequential analysis of randomized controlled trials. Infect. Dis. 53, 691–699. https://doi.org/10.1080/23744235.2021.1923799.

Okoli, G.N., Reddy, V.K., Lam, O.L.T., Askin, N., Rabbani, R., 2024. Update on efficacy of the approved remdesivir regimen for treatment of COVID-19: a systematic review with meta-analysis and trial sequential analysis of randomized controlled trials. Curr. Med. Res. Opin. 40, 1277–1287. https://doi.org/10.1080/03007995.2024.2366443.

Parienti, J.-J., Prazuck, T., Peyro-Saint-Paul, L., Fournier, A., Valentin, C., Brucato, S., Verdon, R., Sève, A., Colin, M., Lesne, F., Guinard, J., Ar Gouilh, M., Dina, J., Vabret, A., Hocqueloux, L., 2021. Effect of Tenofovir Disoproxil Fumarate and emtricitabine on nasopharyngeal SARS-CoV-2 viral load burden amongst outpatients with COVID-19: a pilot, randomized, open-label phase 2 trial. EClinicalMedicine 38, 100993. https://doi.org/10.1016/j.eclinm.2021.100993.

Pettersen, E.F., Goddard, T.D., Huang, C.C., Couch, G.S., Greenblatt, D.M., Meng, E.C., Ferrin, T.E., 2004. UCSF chimera—A visualization system for exploratory research and analysis. J. Comput. Chem. 25, 1605–1612. https://doi.org/10.1002/jcc.20084.

Ray, A.S., 2005. Intracellular interactions between nucleos(t)ide inhibitors of HIV reverse transcriptase. AIDS Rev. 7, 113–125.

Schimunek, J., Seidl, P., Elez, K., Hempel, T., Le, T., Noé, F., Olsson, Simon, Raich, L., Winter, R., Gokcan, H., Gusev, F., Gutkin, E.M., Isayev, O., Kurnikova, M.G., Narangoda, C.H., Zubatyuk, Roman, Bosko, I.P., Furs, K.V., Karpenko Anna, D., Kornoushenko, Y.V., Shuldau, M., Yushkevich, A., Benabderrahmane, M.B., Bousquet-Melou, P., Bureau, R., Charton, B., Cirou, B.C., Gil, G., Allen, W.J., Sirimulla, S., Watowich, S., Antonopoulos, Nick, Epitropakis, N., Krasoulis, A., Itsikalis, V., Theodorakis, S., Kozlovskii, I., Maliutin, A., Medvedev, A., Popov, Petr, Zaretckii, M., Eghbal-Zadeh, H., Halmich, C., Hochreiter, S., Mayr, A., Ruch, Peter, Widrich, M., Berenger, F., Kumar, Ashutosh, Yamanishi, Y., Zhang, K.Y.J.,

Bengio, Emmanuel, Bengio, Y., Jain, M.J., Korablyov, M., Liu, C.-H., Marcou, G., Glaab, E., Barnsley, K., Iyengar, S.M., Ondrechen, Mary Jo, Haupt, V.J., Kaiser, F., Schroeder, Michael, Pugliese, L., Albani, S., Athanasiou, Christina, Beccari, A., Carloni, P., D'Arrigo, G., Gianquinto, E., Goßen, J., Hanke, A., Joseph, B.P., Kokh, D. B., Kovachka, S., Manelfi, C., Mukherjee, G., Muñiz-Chicharro, A., Musiani, F., Nunes-Alves, A., Paiardi, G., Rossetti, G., Sadiq, S.K., Spyrakis, F., Talarico, C., Tsengenes, A., Wade, R.C., Copeland, C., Gaiser, J., Olson, D.R., Roy, A., Venkatraman, V., Wheeler, T.J., Arthanari, H., Blaschitz, K., Cespugli, M., Durmaz, V., Fackeldey, K., Fischer, P.D., Gorgulla, C., Gruber, C., Gruber, K., Hetmann, M., Kinney, J.E., Padmanabha Das, K.M., Pandita, S., Singh, A., Steinkellner, G., Tesseyre, G., Wagner, G., Wang, Z.-F., Yust, R.J., Druzhilovskiy, D. S., Filimonov, D.A., Pogodin, P.V., Poroikov, V., Rudik Anastassia, V., Stolbov, L.A., Veselovsky, A.V., De Rosa, M., De Simone, G., Gulotta, M.R., Lombino, J., Mekni, N., Perricone, U., Casini, Arturo, Embree, A., Gordon, D.B., Lei, D., Pratt, K., Voigt, C.A., Chen, K.-Y., Jacob, Y., Krischuns, T., Lafaye, P., Zettor, A., Rodr\'\iguez, M.L., White, K.M., Fearon, D., Von Delft, F., Walsh, M.A., Horvath, D., Brooks 3rd, C.L., Falsafi, Babak, Ford, B., Garc\'\ia-Sastre, A., Yup, Lee Sang, Naffakh, N., Varnek, A., Klambauer, G., Hermans, T.M., 2024. A community effort in SARS-CoV-2 drug discovery. Mol. Inf. 43, e202300262.

Shelley, J.C., Cholleti, A., Frye, L.L., Greenwood, J.R., Timlin, M.R., Uchimaya, M., 2007. Epik: a software program for pK a prediction and protonation state generation for drug-like molecules. J. Comput. Aided Mol. Des. 21, 681–691. https://doi.org/10.1007/s10822-007-9133-z.

Singh, D., Kushwaha, T., Kulandaisamy, R., Kumar, V., Baswal, K., Tiwari, S.H., Ghorai, A., Kumar, M., Kumar, S., De, S., Polamarasetty, A., Sehgal, D., Katika, M.R., Gadde, S., Côté, M., Kayampeta, S.R., Appaiahgari, M.B., Inampudi, K.K., 2025. Redefining NSP12 activity in SARS-CoV-2 and its regulation by NSP8 and NSP7. Mol. Ther. Nucleic Acids 36, 102452. https://doi.org/10.1016/j.omtn.2025.102452.

Smith, E.C., Blanc, H., Vignuzzi, M., Denison, M.R., 2013. Coronaviruses lacking exoribonuclease activity are susceptible to lethal mutagenesis: evidence for proofreading and potential therapeutics. PLoS Pathog. 9, e1003565. https://doi.org/10.1371/journal.ppat.1003565.

Stefanelli, I., Corona, A., Cerchia, C., Cassese, E., Improta, S., Costanzi, E., Pelliccia, S., Morasso, S., Esposito, F., Paulis, A., Scognamiglio, S., Di Leva, F.S., Storici, P., Brindisi, M., Tramontano, E., Cannalire, R., Summa, V., 2023. Broad-spectrum coronavirus 3C-like protease peptidomimetic inhibitors effectively block SARS-CoV-2 replication in cells: design, synthesis, biological evaluation, and X-ray structure determination. Eur. J. Med. Chem. 253, 115311. https://doi.org/10.1016/j.ejmech.2023.115311.

Steiner, S., Kratzel, A., Barut, G.T., Lang, R.M., Aguiar Moreira, E., Thomann, L., Kelly, J. N., Thiel, V., 2024. SARS-CoV-2 biology and host interactions. Nat. Rev. Microbiol. 22, 206–225. https://doi.org/10.1038/s41579-023-01003-z.

Vuong, W., Khan, M.B., Fischer, C., Arutyunova, E., Lamer, T., Shields, J., Saffran, H.A., McKay, R.T., van Belkum, M.J., Joyce, M.A., Young, H.S., Tyrrell, D.L., Vederas, J.C., Lemieux, M.J., 2020. Feline coronavirus drug inhibits the main protease of SARS-CoV-2 and blocks virus replication. Nat. Commun. 11, 4282. https://doi.org/10.1038/s41467-020-18096-2.

Wang, X., Sacramento, C.Q., Jockusch, S., Chaves, O.A., Tao, C., Fintelman-Rodrigues, N., Chien, M., Temerozo, J.R., Li, X., Kumar, S., Xie, W., Patel, D.J., Meyer, C., Garzia, A., Tuschl, T., Bozza, P.T., Russo, J.J., Souza, T.M.L., Ju, J., 2022. Combination of antiviral drugs inhibits SARS-CoV-2 polymerase and exonuclease and demonstrates COVID-19 therapeutic potential in viral cell culture. Commun. Biol. 5, 154. https://doi.org/10.1038/s42003-022-03101-9.

World Health Organization, 2025. WHO COVID-19 dashboard [WWW Document]. https://data.who.int/dashboards/covid19.

Yang, Y., Li, Y., Becker, S.T., Khan, A., Luo, G., Liu, B., Liu, C., 2025. Molecular basis of SARS-CoV-2 proofreading enzyme–mediated resistance to remdesivir. In: Proceedings of the National Academy of Sciences, 122. https://doi.org/10.1073/pnas.2519755122.

Yin, W., Luan, X., Li, Z., Zhou, Ziwei, Wang, Q., Gao, M., Wang, X., Zhou, F., Shi, J., You, E., Liu, M., Wang, Q., Jiang, Y., Jiang, H., Xiao, Gengfu, Zhang, L., Yu, X., Zhang, S., Eric Xu, H., 2021. Structural basis for inhibition of the SARS-CoV-2 RNA polymerase by suramin. Nat. Struct. Mol. Biol. 28, 319–325.

Zhao, C., Weber, S., Schols, D., Balzarini, J., Meier, C., 2020. Prodrugs of γ-Alkyl-Modified nucleoside triphosphates: improved inhibition of HIV reverse transcriptase. Angew. Chem. Int. Ed. 59, 22063–22071. https://doi.org/10.1002/anie.202003073.

Zur, M., Peselev, T., Yanko, S., Rotshild, V., Matok, I., 2024. Efficacy and safety of antiviral treatments for symptomatic COVID-19 outpatients: systematic review and network meta-analysis. Antivir. Res. 221, 105768. https://doi.org/10.1016/j.antiviral.2023.105768.